A novel rigidizable inflatable lunar habitation system design concept and material characterization

Wang, Qinyu; Feng, Peng; Jansen, Kaspar; Bao, Charun

DOI
10.1016/j.matdes.2024.113289

Publication date
2024

Document Version
Final published version

Published in
Materials and Design

Materials & Design 246 (2024) 113289

Contents lists available at ScienceDirect

Materials & Design

journal homepage: www.elsevier.com/locate/matdes

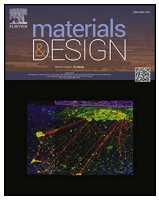

A novel rigidizable inflatable lunar habitation system: design concept and material characterization

Qinyu Wang [a], Peng Feng [a,*], Kaspar Jansen [b], Charun Bao [a]

[a] Key Laboratory of Civil Engineering Safety and Durability of China Education Ministry, Department of Civil Engineering, Tsinghua University, Beijing 100084, China
[b] Department of Design Engineering, TU Delft, 2628 CE Delft, Netherlands

ARTICLE INFO

Keywords:
Lunar construction
Inflatable lunar habitat
Shape memory polymer (SMP)
Rigidization technology
Structure property
Construction process
Material characterization

ABSTRACT

Constructing lunar bases is crucial as lunar missions progress towards utilization and exploitation. The challenging lunar environment, with its unique characteristics and limited resources, requires special materials, structures, and construction methods. Inflatable structures offer great potential for lunar construction due to their advantages in transportation, stowage, construction, and reliability. This paper proposes a rigidizable inflatable lunar habitat that maintains its shape even after air leakage, enhancing safety, durability, and fixability. The membrane material adapts to different requirements during transportation, construction, and service, achieved through solid-state actuation of shape memory polymer (SMP) for stiffness variation, allowing multiple moves and ground tests. This work comprises three parts: 1) system: design concept and construction processes, 2) material: design and characterization of restraint and rigidization materials, and 3) structure: numerical validation of structure properties. Finite element analysis, based on material models obtained through dynamic mechanical analysis (DMA) and tensile tests, demonstrates the effectiveness of including an SMP rigidization layer in preventing collapse and enhancing dynamic properties. This paper not only proposes a new system, but also provides material design methods and requirements, along with structural validation techniques. Findings validate the feasibility of rigidizable inflatable lunar habitats, applicable in extreme environments, also in temporary buildings, space structures, and soft robotics.

1. Introduction

The Moon is crucial for human exploration and technological advancements, serving as a stepping stone for future missions to Mars and beyond. Lunar exploration offers significant opportunities for scientific research, energy production, and resource development. It also promotes international cooperation and has commercial potential, including space tourism [1]. Driven by the demanding space activities and breakthrough in space technologies, recent years have seen a resurgence of global interest in lunar exploration [2], with initiatives like NASA's Artemis Program and the International Lunar Research Station (ILRS) [3] by China and Russia. Other countries like Europe [4,5], Japan [6,7], South Korea [8], and India are also actively involved in lunar explorations, launching lunar probes, and conducting scientific research.

As lunar missions shift from exploration towards exploitation and utilization, constructing lunar bases has become a crucial objective for future missions. However, the challenging lunar environment, with its unique characteristics such as low gravity, ultra-high vacuum, temperature variations, radiation, and limited resources, demands special materials, structures, and construction methods. Extensive research has led to various proposed construction schemes. NASA's SinterHub combines deployable membrane structures, pre-integrated rigid elements, and a sintered regolith shell [9]. ESA's Lunar Outpost incorporates a core cabin, inflatable structure, and protective shell using Sorel cement solidified lunar regolith and D-shape technology [10]. Huazhong University of Science and Technology (HUST) proposed the Xuanwu lunar habitation scheme, which utilizes in-situ prepared lunar regolith bricks and internal membrane structures [11]. These schemes share common features, such as using in-situ materials for protective shells and employing membrane structures to establish a habitable environment. A typical mode of lunar habitats consists of three main parts: prefabricated core module, inflatable structure, and in-situ material structure. By repurposing landers into a core functional area, on-site operations are reduced through the reuse of life support devices and protective systems. Inflatable structures expand the available space, providing high

* Corresponding author.
E-mail address: fengpeng@tsinghua.edu.cn (P. Feng).

https://doi.org/10.1016/j.matdes.2024.113289
Received 5 May 2024; Received in revised form 15 August 2024; Accepted 1 September 2024
Available online 2 September 2024

deployment ratios, airtightness, and activity areas for astronauts. The outer structures, made from in-situ materials, such as compacted regolith, regolith blocks, lunar concrete, or regolith bags [12], serve as protective shells or self-supporting structures [13].

This research focuses on the part of inflatable structures, which are widely used in space capsule designs and hold great potential for lunar habitation modules [14], considering transportation, storage, construction, and reliability. This project proposes a new type of rigidizable inflatable lunar habitats that maintain their shapes even after puncture or air leakage, significantly enhancing safety, durability, and fixability. By adjusting material properties, the stiffness of the membrane can be selectively increased after inflation, allowing the structure to meet specific requirements during transportation, construction, and service life. This research paper covers three main parts. Section 2 focuses on the conceptual design and construction scheme of the rigidizable inflatable lunar habitation system. Sections 3 and 4 delve into the material design and characterization of the restraint and rigidization materials through experimental testing. Section 5 verifies the structure properties through numerical investigations using Finite Element Analysis (FEA). This investigation includes static and modal analyses, using the material models obtained from experimental testing. The rigid and nonrigid cases are evaluated to validate the rigidization capability. Finally, Section 6 and Section 7 conclude this paper and propose future research directions.

2. Concept of rigidizable inflatable habitation system

Inflatable structures offer great potential for lunar construction due to their advantages in transportation, stowage, construction, and reliability. These structures require adaptability to different conditions: the material should be soft for efficient folding and stowage, yet rigid enough to bear structural loads once unfolded. Air inflation can make the membrane structure have a certain rigidity in the limited time after unfolding. However, air leakage is inevitable due to material permeability, connections, and punctures. To enhance long-term structural rigidity, rigidization technologies for membrane structures are necessary. Rigidized membrane structures reduce dependence on air pressure control and continuous inflation, maintain shapes even after puncture and air leakage, prevent collapse, and greatly improve structural safety, durability, and repairability.

Defoort, B. et al. [15] reviewed the rigidization technologies used in space gossamer structures (satellite antennae, solar sails, etc.), which can be classified into three major categories: mechanical, physical, and chemical rigidization. Mechanical rigidization is achieved by inflating and stretching a polymer/aluminum metal film to its yield strain, creating pre-compressive stresses in the metal layer and pre-tensile stresses in the polymer layer to enhance structure stiffness. Chemical rigidization involves temperature or UV-induced polymerization of the resin, while physical rigidization utilizes phase change in the material. Among them, physical rigidization methods are the most commonly used due to their simplicity, reversibility of the rigidization process, low energy requirements, and short maintenance time compared to thermal curing, and allowing for ground testing and multiple applications [15,16]. Shape memory polymers and their composites (SMPs and SMPCs) fall in the physical category. SMPs offer several advantages as rigidization materials for membrane structures, such as high compaction rates, high design flexibility, and simplified design without hinges or mechanical connections at nodes. Moreover, the shape memory function of SMPs has garnered significant attention in space foldable structures, particularly in precision structures where component shape directly affects functionality [17]. This section proposes a conceptual design and construction process for inflatable habitats based on SMP rigidization method.

2.1. Design concept

2.1.1. Expandable configurations for large lunar base construction

Inflatable habitats are commonly shaped based on pressure vessels, such as spheres, cylinders, or their derivatives [18,19]. In this design proposal, a classical ball-and-stick model is employed, incorporating cylindrical and spherical basic units depicted in Fig. 1(a) and (b). The cylindrical units are limited to a maximum of two airlock connections, serving as connection and transit modules. Spherical units, on the other hand, can accommodate multiple airlocks at different angles, allowing for the connection of multiple corridors. By combining these unit types, various architectural complexes can be formed, and additional modules can be added to existing configurations for easy expansion into larger bases, as illustrated in Fig. 1(c)–(e).

2.1.2. Lunar habitat design

The habitats proposed in the paper are designed as follows:

- Inner inflatable structure providing living and research spaces for astronauts.
- Outer regolith layer (compact regolith, regolith bricks, or regolith bags) [12,13] for radiation protection, thermal insulation, and micrometeoroid impact resistance.

Fig. 2 shows the 3D diagrammatic drawing of constructing regolith bricks on the rigidized inflatable structure using robotic arms, where blue parts represent SMP components in the glassy state (high stiffness).

2.2. Construction process

Before establishing a habitable artificial environment on the Moon, human activities are severely restricted, rendering movement nearly impossible. Consequently, a construction approach integrating robots and humans is essential in lunar base design. Initially, a large number of automated and remotely operated robots will be employed for construction, with humans primarily responsible for controlling these robots. Once the habitat module is completed, human activities mainly shift towards base maintenance, scientific research, and base expansion with enhanced facilities [20]. Therefore, the acceleration of sustainable construction and broader lunar exploration relies on automated construction methods that utilize automation and remotely operated robots for construction and resource collection [21].

The key to lunar construction is the design of structural plans and construction processes that overcome challenges like extreme lunar conditions, limited resources, and labor shortages. In automated construction, it is essential to define construction steps and tasks for each stage and establish explicit requirements for robot design, including function, size, carrying capacity, and energy demand. These requirements encompass various activities such as excavation, transportation, assembly of regolith bricks/bags, sintering, and inflation. Construction robots can adopt a combination of “one robot for multiple tasks” and “multiple robots for collaboration” approaches. The first method applies robots equipped with various end-effectors to perform multiple functions, while the second method requires seamless collaboration among swarm robots to execute large-scale construction activities or production lines, with each category of robots assigned to a specific task. The construction process for the proposed rigidizable inflatable habitat is well-defined, with construction robots actively participating in the main steps. The preliminary design and construction process outlined in this study include the following four main steps, as shown in Fig. 3, where blue and red marks represent the glassy state (high stiffness) and the rubbery state (low stiffness) of SMP. When under glass transition temperature T_g, SMP is at the glassy state where the modulus is around 1GPa; when at an elevated temperature above T_g, SMP enters the rubbery state. Stiffness variation between the two states can reach up to 1000 times.

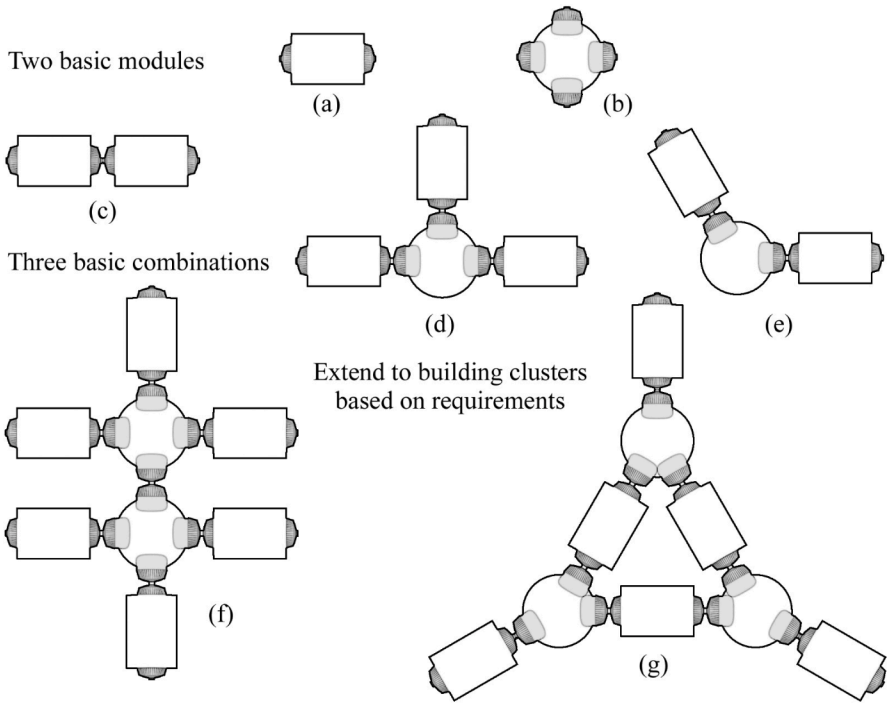

Fig. 1. Extendable lunar base concept (top view): (a) and (b) spherical and cylindrical modules;(c)~(e)three basic combinations; and (f) and (g) two examples of building clusters consisting of multiple modules based on requirements.

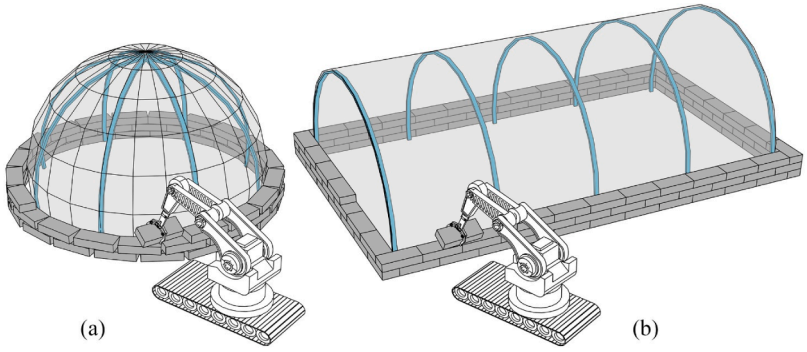

Fig. 2. Diagrammatic drawing of 3D structures, where blue parts represent SMP components in the glassy state: (a) semi-sphere; (b) semi-cylinder or arch. (For interpretation of the references to colour in this figure legend, the reader is referred to the web version of this article.)

- **Inflation & expansion:** The rigidization material initially exists in a highly rigid glassy state, which allows the structure to keep the folded shape tightly for stowage and transportation. When SMP is actuated to the rubbery state, the membrane becomes flexible again, which allows the structure to be inflated and erected. This step may require a transport robot to extract the folded structure, place it accurately in position and orientation, and initiate the inflation process.
- **Rigidization:** Then, SMP enters the glassy state and keeps the inflated shape, resulting in a significant stiffness increase of this inflatable structure. This is the SMP-based rigidization process, which is reversible. Note that for structures that need multiple deployments, after rigidization, by actuating SMP above T_g, the structure can be folded again and reused, achieving a folding and inflation circulation, as shown in Fig. 3(a).
- **Regolith coverage:** For inflatable lunar habitats, the regolith layer is added to cover the rigidized inflatable structure. The rigidized inflated structure serves as a formwork for construction robots to form a compacted regolith layer or assemble regolith bags or bricks. The production process requires robots to solidify and form lunar regolith, which can be referred to our other research [12,13].
- **Pressurization:** The inflated structure is pressurized by adding air again to compensate and maintain a pressure of 1 atmosphere (1 atm), providing a habitable space for human activities. as shown in Fig. 3(b).

2.3. Form finding methods of inflatable structures using SMP/SMPC

Two main form finding methods for inflatable structures with an integrated inner framework consisting of SMP/SMPC can be identified: 1) self-forming SMP frame supporting membrane structure, and 2) membrane structure as formwork to shape SMP frame. Fig. 4 shows the principle behind the two methods.

2.3.1. Self-forming SMP frames supporting membrane structure

In the first category, the inner frame has the ability to self-form into specific shapes. The shaped frame then supports the outer membrane, creating a complete structure. This concept can be compared to the mechanism of an umbrella, which can be found widely in mechanical

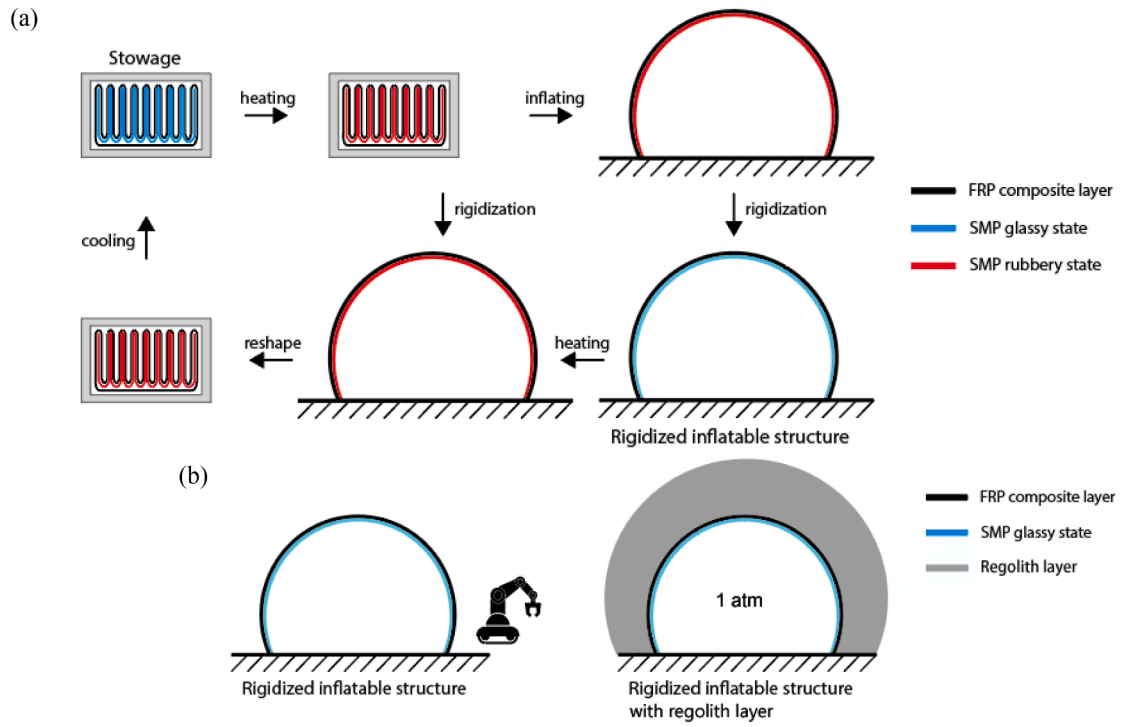

Fig. 3. Construction process: (a) folding & stowage and inflation & expansion circulation of a rigidizable inflatable structure; (b) regolith coverage and pressurization process on rigidized inflatable structure.

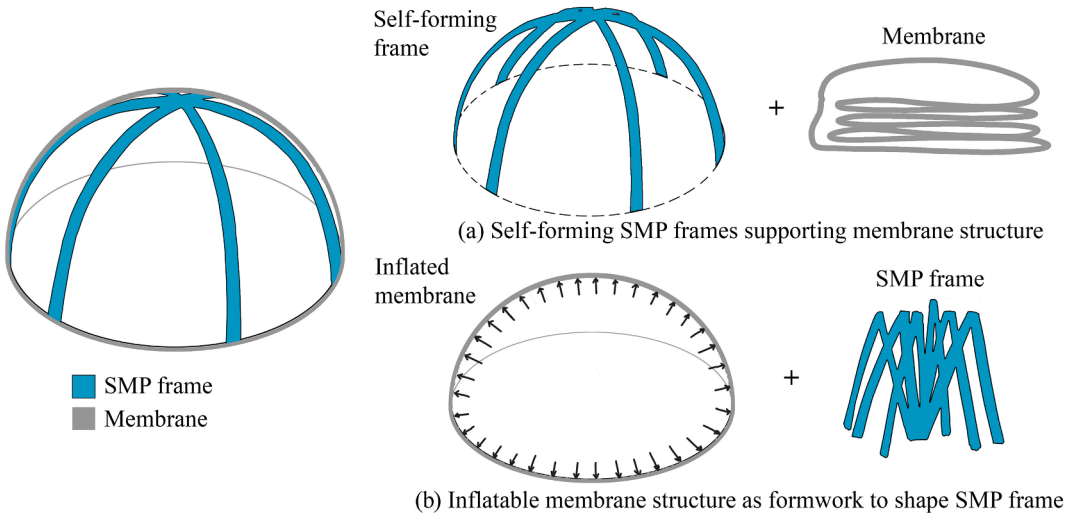

Fig. 4. Form finding methods of inflatable structures using SMP/SMPC: (a) self-forming SMP frames supporting membrane structure; (b) membrane structure as formwork to shape SMP frame.

deployment systems. Fig. 4(a) illustrates the principle behind this category. Li et al. proposed an integral structural design for a lunar base that utilizes the shape recovery property to enable the SMP frame to automatically expand when activated [22]. However, note that SMPs are typically used in small-scale applications like sensors or actuators. For large inflatable structures, SMPs have limited shape memory capability, and it remains uncertain whether SMPs alone can achieve automatic deployment at the scale of a lunar habitat. In such cases, additional actuation systems like shape memory alloys (SMAs) or linear actuators may be required to facilitate shape reconfiguration. Nevertheless, the shape recovery capability of SMPs can greatly reduce residual strains and stresses following deformation in deployable structures.

2.3.2. Membrane structure as formwork to shape SMP frame

In this approach, the inflatable structure serves as formwork to shape the frame. The flexible-state frame, which is attached to the membrane, can be easily deformed and shaped along with the inflatable structure when the SMP is in its rubbery state. Once the SMP is triggered to enter a glassy state, the frame becomes rigid, effectively locking the deformed shape in place, as depicted in Fig. 4(b). In this study, the inflatable membrane structure is used, however, in other applications, other shaped membrane structures like tensioned membrane can also be applied. This technique of using membrane as formwork has been successfully employed in the construction of spray concrete and ice structures [23]. The advantage of this approach is that it eliminates the need for additional actuators to achieve shape reconfiguration, resulting in a more

streamlined and simplified design for shaping the structure. This design concept aligns with the development of rigidizable lunar habitats in this research.

2.4. Distribution of rigidization material

The stiffening capacity of the structure and the energy required for activation depend on the quantity and arrangement of rigidization materials. SMP materials can be incorporated into the rigidization layer in three different forms: surface (SMP/SMPC shell), line (SMP frame), and point (SMP joints & FRP rods). In the "surface" form, SMP materials create a thin shell structure or directly adhere as SMPC to the flexible AFRP restraint layer. In the "line" and "point" forms, an internal framework is formed. The key difference is that the "line" form uses SMP to make the structural members, while the "point" form utilizes SMP joints to connect the composite members and establish the framework. Fig. 5 provides an illustration of these three forms of the rigidization layer.

The figure presented here is for illustrative purpose only and does not depict the final optimized layout. Further research and design are necessary to refine the specific arrangement. The main objective of this paper is to introduce the concept of rigidizable inflatable habitats and evaluate their feasibility. Subsequent numerical studies will primarily focus on the "surface" form.

By utilizing SMP resin, the SMPC skin can form a strong bond with flexible AFRP and also connect additional rods, as depicted in Fig. 6. The rods represent the internal stiffening framework in the "line" or "point" configurations, which can be composed of SMP rods/tubes or FRP rods/tubes with SMP joints. The proportions shown in the figure are not to scale, and further design is needed to address the specifics. Additionally, the actual laminate may be thinner in practice.

3. Characterization of restraint material: flexible AFRP

In 1997, NASA initiated the TransHab project with the goal of developing a cost-effective and spacious capsule for astronauts in space stations. The TransHab capsule comprises a skin system with five functional layers: inner liner, bladder, restraint layer, micrometeoroid/orbital debris protection layer, and thermal protection layer. The skin material should be lightweight, flexible, resistant to high temperatures and radiation, airtight, and easily rigidizable [24,25]. The restraint layer, typically made of high-performance fiber fabrics like Kevlar and Vectran, supports internal air pressure [14].

In this design, the focus primarily lies on the restraint layer, as the regolith layer takes over the functions of micrometeoroid, radiation, and thermal protection. The membrane material comprises a flexible aramid fiber reinforced polymer (AFRP) restraint layer and an SMP rigidization layer. Kevlar is preferred in this project due to its availability and cost-effectiveness compared to the less common Vectran fiber. The AFRP, composed of Kevlar fiber and flexible epoxy resin, handles the primary tension load. By strategically adjusting the material properties of smart materials like SMP/SMPC, the membrane's stiffness can be selectively increased after inflation. This feature allows the structure to meet specific requirements during transportation, construction, and service life by facilitating reversible transitions between glassy and rubbery states.

To design a flexible AFRP composite skin, a comprehensive study encompassing three different resins and multiple fabric options was conducted. Uniaxial tensile tests were performed on AFRP specimens with varying parameters such as component materials, layer numbers, and fabric laying directions. Additionally, dynamic mechanical analysis (DMA) tests were conducted to evaluate the viscoelastic properties, specifically the variation of storage modulus over temperature, of the resins and single-layer AFRPs. Fig. 7 illustrates the experimental framework employed for the uniaxial tensile tests and DMA tests, crucial for designing and characterizing the flexible AFRP restraint layer.

Initially, the flexible epoxy resin EF80 from Easy Composite (UK) and various aramid fiber fabrics (including Kevlar 60 g plain/twill, 110 g plain, and 200 g plain) were selected for fabricating the flexible AFRP composite. Based on the initial trials, it was observed that the 60 g plain weave fabric exhibited higher strength and elastic modulus compared to the 60 g twill weave fabric. However, the single-layer 60 g fabrics were deemed to be too flimsy and prone to deformation during operation. Conversely, the 200 g fabric displayed superior strength and modulus but was too thick to conform to complex curved surfaces. Consequently, the 110 g fabric was chosen for further testing in this research.

In addition to EF80, two more flexible epoxy resins, namely 3016LV (*Hasuncast,USA*) and YH2130 (*Boqiao,China*) were used for DMA tests. Considering factors such as curing conditions, mechanical properties, and price, EF80 was not selected for further study. Tensile tests were conducted on AFRP specimens fabricated with 3016LV and YH2130, considering variations in layer numbers, resin types, folding, and ply orientation. Subsequently, DMA tests were performed on small AFRP specimens, including single-layer specimens tested under tensile mode and four-layer specimens tested under bending mode. These tests aimed to acquire information on the modulus variation with temperature and folding capacity of the AFRP composites.

To design an isotropic elastic material, tensile tests were conducted on big AFRP specimens with different fabric layouts, including variations in layer numbers and laying directions. The objective of these tests was to assess the mechanical properties and performance of the AFRP composites with various fabric configurations.

3.1. Test equipment

Fig. 8 displays the test setups. In both figures, the left side represents the testing machine, while the right side shows a clamped specimen in position. All the tensile tests adhered to the ASTM D3039 standard, employing a displacement rate of 2 mm/min. The tests were conducted using a 100kN Instron tester, as depicted in Fig. 8(a). The Instron tester was equipped with a non-contact video extensometer to measure strain

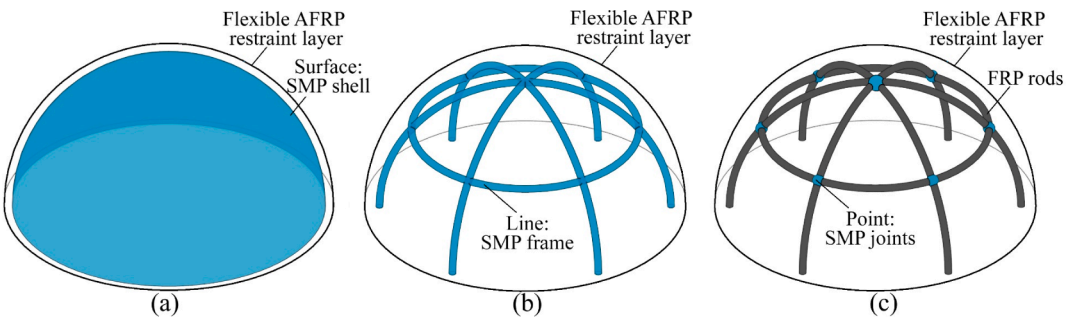

Fig. 5. Three forms of SMP rigidization layer: (a) surface (SMP/ SMPC shell); (b) line (SMP frame); and (c) point (SMP joints & FRP rods).

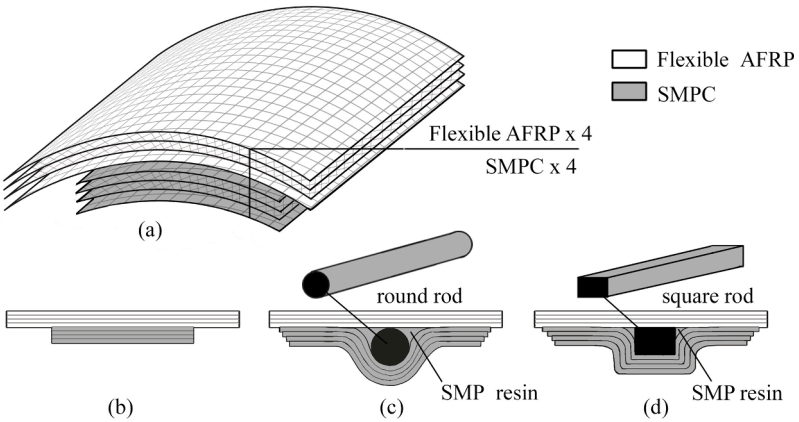

Fig. 6. Connection between SMP and flexible AFRP:(a) 4-layer flexible AFRP with SMPC laminates; (b) cross-section of laminates; and (c) and (d) schematics of connections with circular and square rods, respectively, where SMP resin can be used to fill the seams.

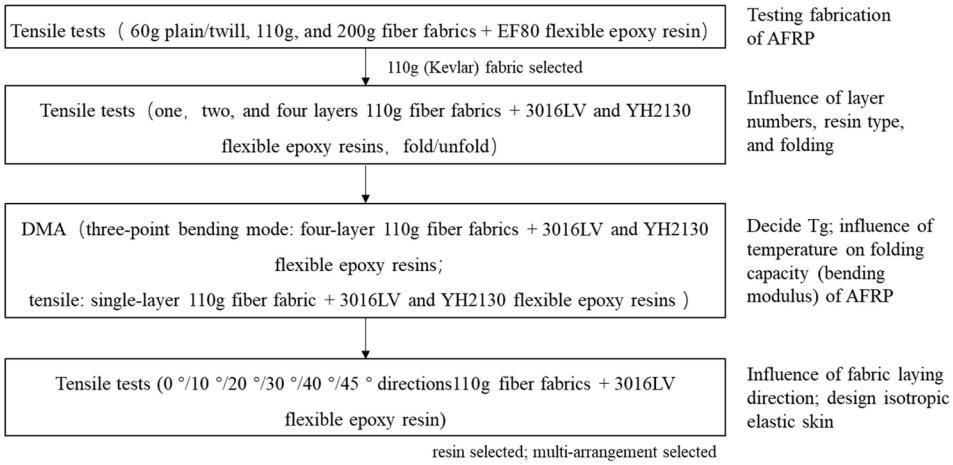

Fig. 7. Framework of uniaxial tensile tests and DMA tests for designing flexible AFRP restraint layer.

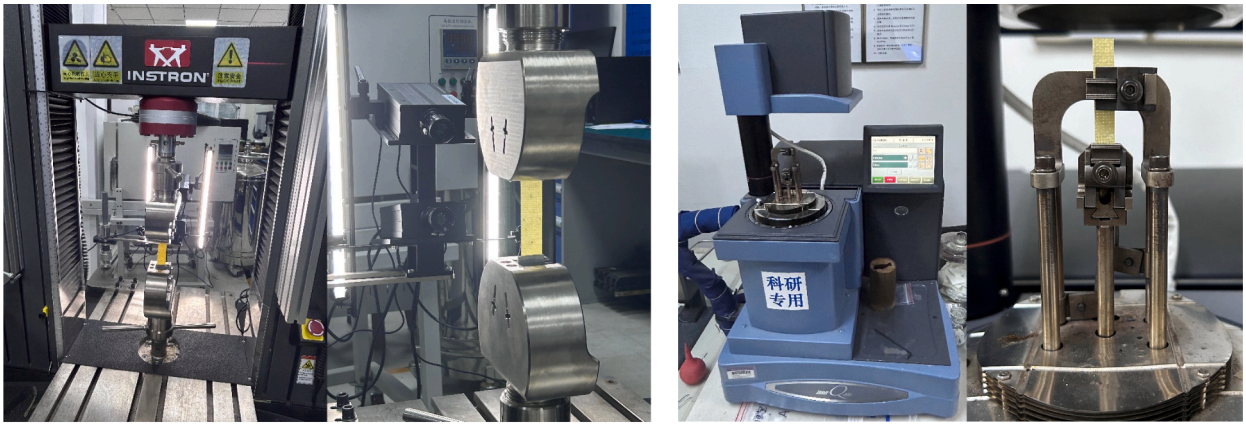

Fig. 8. Test setups: (a) tensile setup at ambient temperature (Instron 100kN); (b) DMA test setup (Q800).

during the tensile tests performed at ambient temperature. On the other hand, the dynamic mechanical analysis (DMA) tests were conducted using a Q800 instrument manufactured by TA Instruments, as illustrated in Fig. 8(b). The DMA setup on the right demonstrates the configuration used for tensile mode of the tests.

3.2. Monotonic uniaxial tensile tests

3.2.1. Tensile tests on 3016LV and YH2130 AFRPs: one, two, and four layers

In the initial tensile tests, two flexible epoxy resins, YH2130 and 3016LV, were chosen to combine 110 g plain woven aramid (Kevlar) fabrics. Eight groups of AFRP specimens were prepared: four groups

using 3016LV and four groups using YH2130. The specimens had dimensions of 200 mm length and 25 mm width, with 60 mm long aluminum bonded tabs at both ends. The thickness of the specimens varied based on the number of fabric layers, ranging from approximately 0.27 mm to 0.8 mm.

The A, B, and C groups corresponded to specimens with one, two, and four layers of aramid fabrics, respectively. The D group consisted of specimens from the C group that were folded in the middle and compressed by clamps for one week before testing. The comparison between the C and D groups aimed to assess the influence of folding on tensile strength. Fig. 9 depicts the photos of 3016LV C and D group specimens.

In general, the stress–strain relationship in the 0° direction of the material was almost linear, exhibiting elasticity followed by sudden rupture before any significant damage occurs. Fig. 10 presents the stress–strain curves of 3016LV and YH230 AFRP specimens, demonstrating the effect of layer numbers on these curves. For one-layer specimens, the single ply material was prone to deformation during manual layup and adhesion of aluminum tabs, which results in unsatisfactory stiffness and strength. Essentially, the specimens tended to fail at the ends and exhibited greater dispersion compared to other multilayer groups. In addition, the per-ply thickness of the A group was generally larger than that of the B and C groups, leading to weaker mechanical strength due to higher resin content and lower fiber volume fraction. The B and C groups, which consists of two and four layers, respectively, exhibited similar stress–strain curves. The average ultimate stresses of the B and C groups for both 3016LV and YH2130 AFRP were 70.9 % and 42.6 % higher than those of the A groups, respectively. Therefore, to investigate the mechanical properties of the material accurately, it is recommended to use at least two layers of fabrics, with more layers yielding better results. In this case, the stress–strain curves from the C groups, which shows the most consistent results, were used to determine the average elastic modulus, ultimate stress, strain, and load. The flexibility of the resin prevented tightening at the beginning of the specimens, potentially leading to an underestimated elastic modulus. To address this, the modulus was computed using the $\Delta\varepsilon = 0.5$ % chord modulus from the middle range of the stress–strain curves. Strain ranges of 1 % to 1.5 % and 0.7 % to 1.2 % yield good results for all 3016LV and YH2130 AFRP specimens, respectively, as shown in Fig. 10.

The test results of all specimens are summarized in Table 1. When comparing the two resin types, it can be observed that the elastic moduli were generally similar, but the ultimate strain, stresses, and loads of 3016LV AFRP were larger than those of YH2130 AFRP. Taking C groups as references, the average elastic modulus of 3016LV and YH2130 AFRP were 1.398GPa and 1.362GPa, respectively. The average ultimate stress and strain for 3016LV AFRP were 2.4 % and 299.4 MPa, respectively, compared to 1.91 % and 243.3 MPa for YH2130 AFRP. The 3016LV groups exhibited approximately 20 % larger ultimate strain, stress, and load compared to the YH2130 groups (20.4 % for strain, 18.7 % for stress, and 22.4 % for load). Although the chord modulus values are influenced by the chosen strain range, they are used as a reference rather than a decisive factor in selecting resin types. Based on the results, 3016LV resin was chosen for the subsequent design and numerical investigation in this research.

Fig. 11(a) displays the failure modes of unfolded and folded 3016LV AFRP specimens. The damage locations of unfolded specimens were unpredictable, occurring in various parts. Typically, the failure initiated at the edge fibers and gradually propagated inward until the crack extended through the transverse section. In contrast, all folded specimens exhibited damage at the crease location, resulting from local stress concentration due to folding.

The average elastic modulus and ultimate stress values of 3016LV AFRP were 1.398 GPa and 299.4 MPa for the C group (unfolded specimens), and 1.145 GPa and 245.1 MPa for the D group (folded specimens), respectively. Folding did affect the stiffness and strength properties of flexible AFRP, resulting in an 18.1 % decrease for both parameters for the 3016LV resin. In the case of YH2130 AFRP, the elastic modulus and ultimate stress decreased by 1.2 % (from 1.362 to 1.345 GPa) and 13.6 % (from 243.3 to 210.3 MPa), respectively.

Despite the outstanding anti-fatigue property of Kevlar fiber and the flexibility of epoxy resin, folding still induces damage and buckling in the resin, as observed in Fig. 11(b). The magnified photograph captured by an electronic magnifier showcases the folding area on AFRP with a 20x magnification. The highlighted white section in the photo indicates the occurrence of local buckling, which is caused by creasing in the resin. The crease appears in a zigzag pattern, as shown in red dashed curve, and in certain instances, micro cracks can also be observed.

3.2.2. *Tensile tests on 3016LV AFRP: different directions*

To investigate the effect of angle, specimens of two-layer 3016LV AFRP were cut at various angles: 0°, 10°, 20°, 30°, 40°, and 45°. Fig. 12 (a) presents the stress–strain curves for these different angles. As the fiber angle increased from 0° to 45°, the specimens exhibited an increasing level of ductility. At 0° fiber direction, the ultimate strain was only 2.4 %, whereas at 45°, the ultimate strain reached as high as 37.7 %. The stress–strain curves for the 0° and 10° orientations demonstrated linear elasticity. However, starting from an angle of 20°, the stress–-strain curves exhibited a change in curvature. As the angle increased to 30°, the tensile curve gradually separated into two distinct stiffness

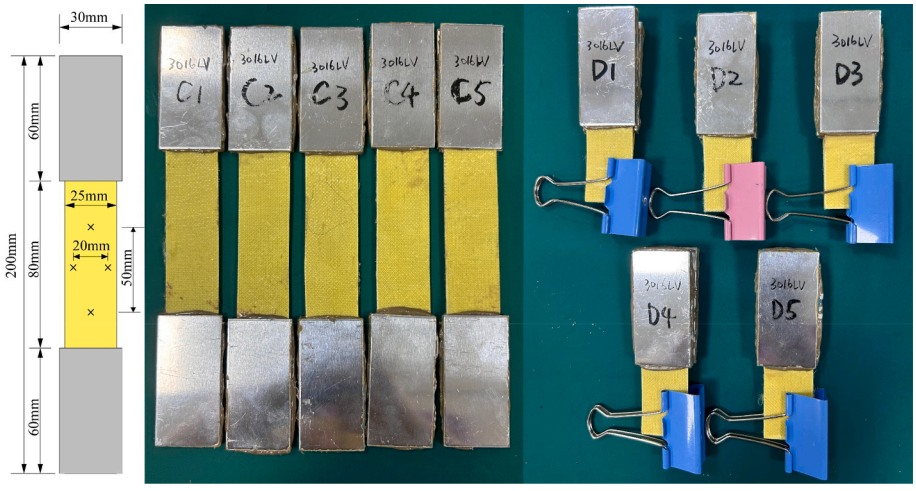

Fig. 9. Tensile test specimens: 3016LV AFRP C and D groups (unfolded and folded).

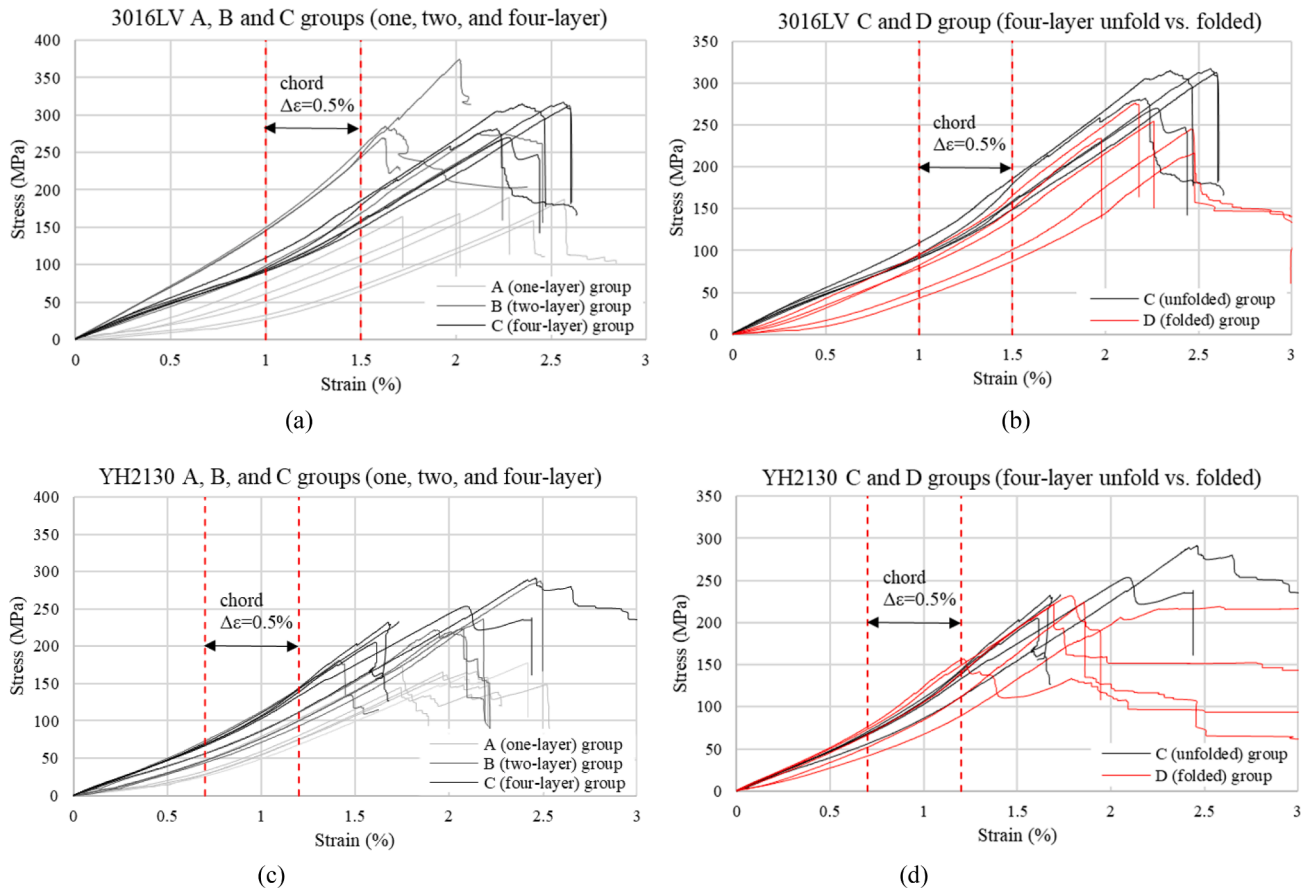

Fig. 10. Stress-stain curves: (a) effect of layer numbers and (b) unfolded C and folded D groups of 3016LV AFRP specimens; (c) effect of layer numbers and (d) unfolded C and folded D groups of YH2130 AFRP specimens.

Table 1
Tensile test results of one, two, and four-layer 3016LV and YH2130 AFRP specimens: elastic modulus, ultimate strain, ultimate stress, and ultimate load.

	Group	Modulus (GPa)	Ultimate Strain (%)	Ultimate Stress (MPa)	Ultimate Load (kN)
3016LV AFRP	A (1-layer)	0.9341	2.20	173.8	1.25
	B (2-layer)	1.748	1.9	294.6	2.64
	C (4-layer)	1.398	2.40	299.4	5.98
	D (4-layer) fold	1.145	2.27	245.1	4.91
YH2130 AFRP	A (1-layer)	0.9541	2.00	165.6	1.11
	B (2-layer)	1.127	2.03	229.9	2.55
	C (4-layer)	1.362	1.91	243.3	4.64
	D (4-layer) fold	1.345	1.76	210.3	3.99

regions. These regions were connected by a platform, and as the angle increased further, the length of the platform between the two stiffness regions also increased.

During the platform stage, the strain continued to increase while the stress remained relatively constant. This behavior could be attributed to the redistribution of the inclined fibers when subjected to axial tensile loading. With more fibers undergoing redistribution, an increasing number of them aligned with the direction of the applied load, resulting in a significant enhancement in the material's stiffness. This stiffening phase persisted until the material reached its ultimate stress. At this point, the redistributed fibers gradually ruptured, ultimately leading to material failure. Since the material is orthotropic, it is possible to plot a complete 360° stress and strain versus angle graph using the results from 0° to 45°. However, in this case, Fig. 12(b) specifically shows the ultimate stress and strain versus angle within the range of 0° to 90° for brevity.

Fig. 13 illustrates the chord modulus, ultimate stress, and ultimate strain of the multi-layer material computed within the range of 1 % to 1.5 %. The chord modulus is shown as the radius-vector in logarithmic scale in Fig. 13(b). Note that despite significant variations in the ultimate stress and strain at different angles, the load-bearing behavior of multi-layer materials composed of different angle layers was primarily influenced by the number of fibers aligned with the loading direction. When multiple layers worked together, the fibers aligned at 0° played a critical role in controlling the overall strain, resulting in an ultimate strain of 2.4 %. Assuming that no delamination occurs and the skin layer functions in coordination until fiber rupture, the overall stiffness of the multi-layer material should be the average stiffness of each layer due to deformation coordination. Similarly, the strength can be calculated as the average stress of each layer when the fibers aligned at 0° fail. The computed results are shown in Table 2.

For numerical investigation in Section 5, an isotropic elastic material model is established for the flexible AFRP in resistance layer. The material properties for this model were determined using classical laminate theory (CLT) in ACP module of Ansys Workbench. The resulting laminate stiffness values obtained from a four-layer stacking sequence [0F/

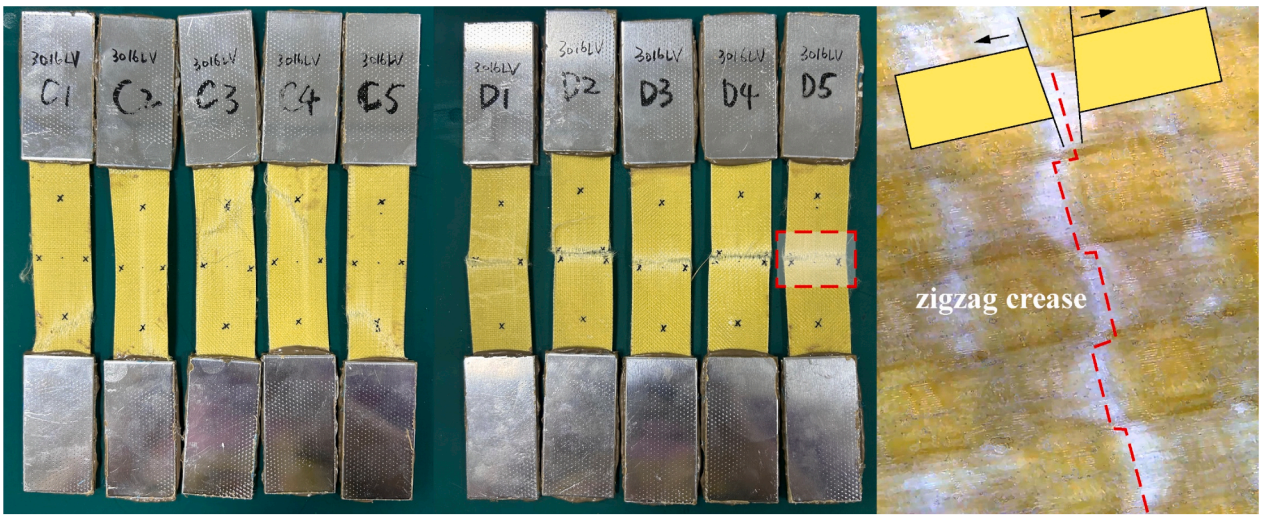

Fig. 11. (a) Failure modes of 3016LV AFRP C and D groups after testing; (b)20x photo, where white parts show the local buckling of the resin.

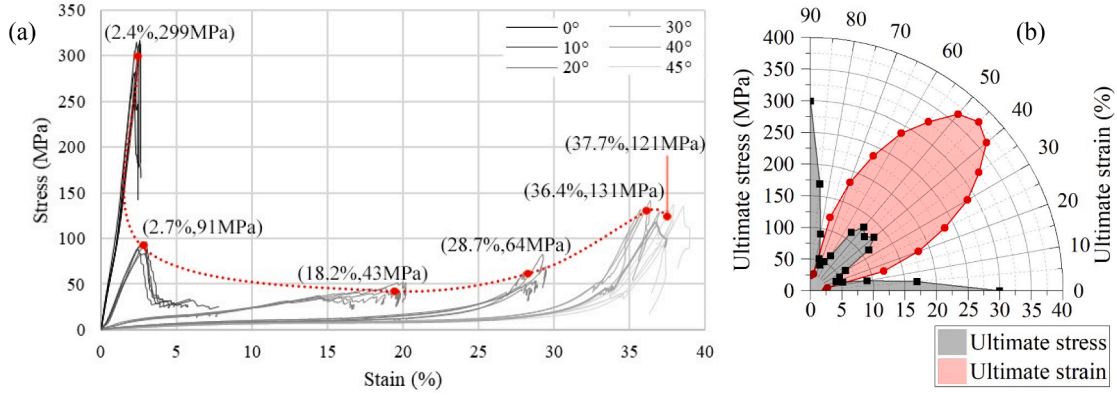

Fig. 12. Stress vs. strain at 0°, 10°, 20°, 30°, 40°, and 45°: (a) full scale (red dots show the average ultimate strain and stress values for different angle groups); (b) stress and strain vs. angle. (For interpretation of the references to colour in this figure legend, the reader is referred to the web version of this article.)

Table 2
1% to 1.5% chord modulus and ultimate stress vs. ply angle of 3016LV AFRP.

	Ply Angle	Modulus (MPa)	Ultimate Strain (%)	Ultimate Stress (MPa)	2.40 % stress (MPa)
3016 LV AFRP	0°	13,976	2.40	299.4	299.4
	10°	4100	2.73	90.93	98.4
	20°	459.0	18.2	43.05	11.0
	30°	146.8	28.7	63.83	3.52
	40°	108.4	36.4	131.4	2.60
	45°	97.98	37.7	120.7	2.35

45F2/0F] were as follows: $E_1 = E_2 = 8543$ MPa and $G_{12} = 2696$ MPa. These values represent the elastic moduli in the fiber direction (E_1) and perpendicular to the fiber direction (E_2), as well as the shear modulus (G_{12}) of the material. For the subsequent numerical investigations, an ultimate stress of 151 MPa (computed as the average of 2.4 % stress of 299.4 MPa at 0° and 2.35 MPa at 45°) and an ultimate strain of 2.4 % were adopted.

3.3. Dynamic mechanical analysis (DMA)

The effect of temperature on material performance was investigated using DMA tests on three resins (EF80, 3016LV, and YH2130) and two AFRPs (3016LV AFRP and YH2130 AFRP). DMA measures the complex modulus, which consists of storage modulus (E′) and loss modulus (E″), representing energy stored in the elastic part and energy dissipated as heat due to friction, respectively.

In the conducted tests, a multi-frequency-strain test was performed with an oscillatory strain of 10 μm. The frequencies ranged from 0.32 Hz to 30 Hz and were spaced logarithmically, with two points per decade (0.32 Hz, 1 Hz, 3 Hz, 10 Hz, and 30 Hz). During each test, the temperature was increased at a constant rate of 1 °C/min from −140 °C to 100 °C. The DMA results for 3016LV resin and AFRP are presented in Fig. 14, while the results for EF80 resin and YH2130 resin and AFRP can be found in Appendix (Figure A1 and Figure A2). As the loading frequency increased, all the E', E″, and Tan δ curves shifted rightward with slightly increased amplitudes. Note that data at 60 Hz exhibited significant noise and was excluded from further analysis for constructing viscoelastic material models.

The glass transition temperature (T_g) of the materials was determined from peak Tan δ values at 1 Hz. The 3016LV and YH2130 resins exhibited a T_g of approximately 20 °C, while the EF80 resin had a T_g of around 30 °C. The addition of fiber fabrics raised T_g, reaching around 50 °C in DMA tensile mode and 23 °C in three-point bending mode. This indicates that the fibers predominantly influenced the elastic modulus in tension, while the resin played a dominant role in bending. Fig. 14*(c)* shows that when the materials were at the rubbery state above T_g, they were highly flexible and easily foldable, demonstrating their folding capability. However, below T_g, the material experienced a significant

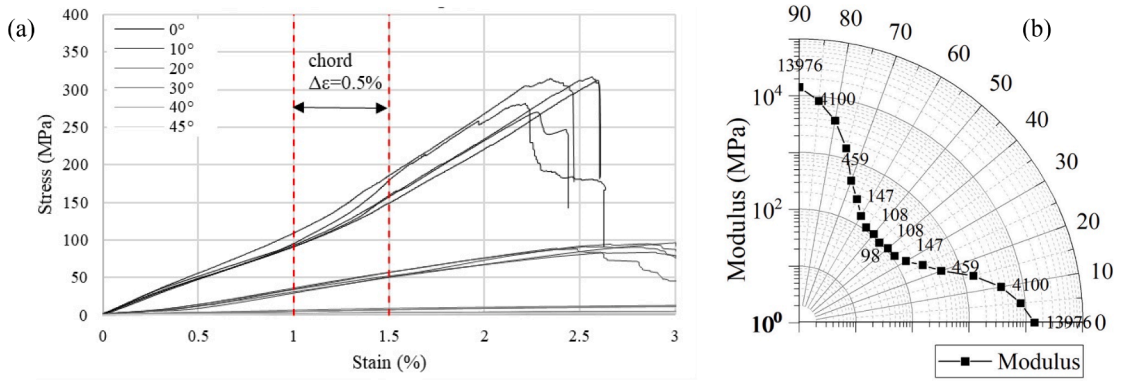

Fig. 13. 3016LV AFRP: (a) stress vs. strain curves at 0°, 10°, 20°, 30°, 40°, and 45° (0 ~ 3 % strain range for modulus calculation); (b) modulus vs. angle.

increase in stiffness.

To further explore the viscoelastic properties of the material, a viscoelastic model was established using 3016LV resin and 3016LV AFRP as examples. The characterization of the viscoelastic model requires two curves: the shift factor curve and the master curve [26]. The shift factor curve represents the change in stress relaxation rate with temperature. On the other hand, the master curve depicts the change in storage modulus over a wide range of frequencies and temperatures. In the linear viscoelastic range, temperature affects the relaxation process by accelerating it without affecting the overall amount of relaxation. Therefore, it is common to model the storage modulus using the equation:

$$E(t,T) = E\left(t_{red}, T_{ref}\right), t_{red} = a_T t, \tag{1}$$

where a_T is the temperature dependent shift factor, t_{red} is the reduced (or shifted) time scale and T_{ref} is an arbitrarily chosen reference temperature. Note that in some literature the reduced time is defined as $t_{red} = t/a_T$.

Fig. 15 illustrates the constructed master and shift factor curves for 3016LV resin and AFRP. The dashed lines bound the storage moduli measured within the frequency range of 0.30 Hz to 10 Hz and the temperature range of −46 °C to 72 °C for 3016LV resin and −47 °C to 85 °C for 3016LV AFRP. At the reference temperature of 20 °C, the shift factor is 1. The moduli at different temperatures and/or frequencies, which were not directly measured through DMA, can be obtained by shifting along the frequency axis using the shift factor curve. For a more comprehensive understanding of obtaining a master curve, readers can refer to the work of Ferry [27] for detailed explanations and

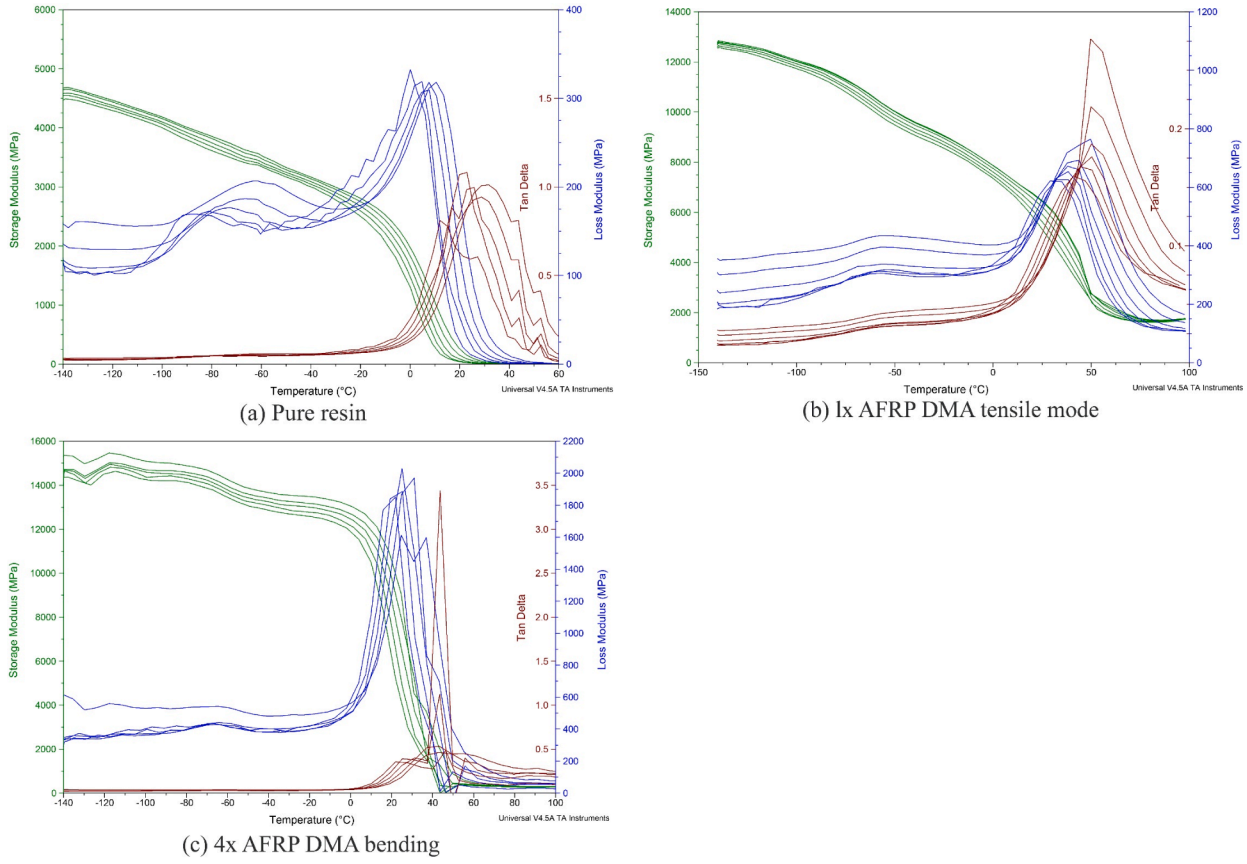

Fig. 14. Storage modulus, loss modulus, and Tan δ vs. temperature for 3016LV AFRP: (a) pure resin, (b) one-layer AFRP under tensile mode, and (c) four-layer AFRP under bending mode.

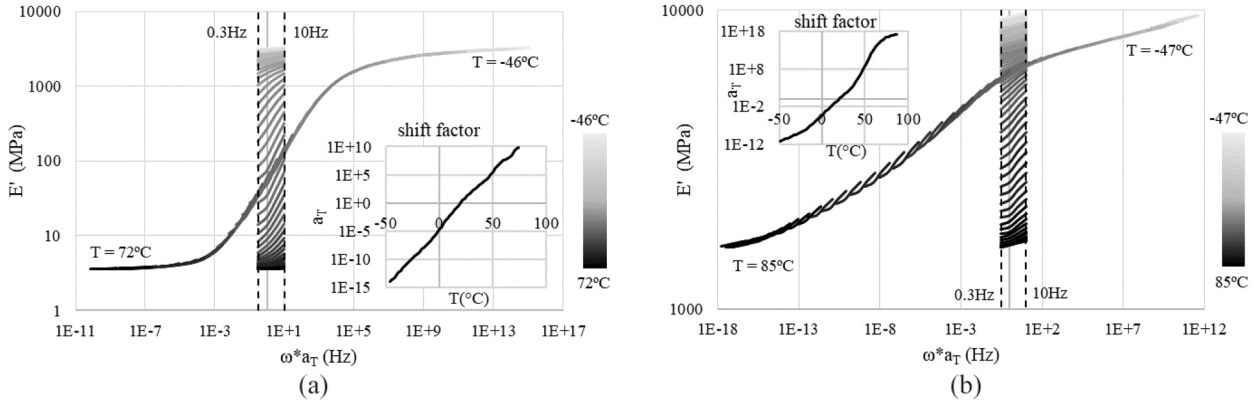

Fig. 15. Master and shift factor curves (T_{ref} = 20 °C):(a) 3016LV resin and (b) one-layer 3016LV AFRP.

methodologies.

This section explored potential materials for the restraint layer of the membrane in rigidizable inflatable lunar habitats. The material needs to be flexible for easy folding and have high tensile strength to bear loads. However, folding can induce local bulking in the resin (even through it is flexible), leading to weakened strength. Folding fatigue is also a concern. Thus, design optimization is necessary. One approach is to incorporate creases without resin to avoid weakening folds caused by accumulated residual stress and strain in the resin at the crease sites.

Besides, it is crucial to note that resin materials transition into a glassy state at extremely low temperatures, particularly in environments like the lunar south pole (a proposed location for lunar bases) [5], where temperatures can plummet to 110 K (−163 °C) [28], rendering the membranes excessively rigid for folding. To ensure successful deployment of inflatable structures, it becomes imperative to utilize resins or coatings with lower T_g and implement temperature control during construction. Coating materials that exhibit exceptional resistance to low temperatures, such as high-phenyl silicone and fluorine rubbers, should be considered. However, it is important to emphasize that the primary focus of this study lies in the conceptual design of rigidizable inflatable habitats, which finds applicability not only in lunar surface scenarios but also in extreme environments like polar regions and plateaus. Consequently, these materials were explored within terrestrial experimental environments. Further research is warranted to evaluate their performance under lunar conditions.

4. Rigidization material: SMP/SMPC

4.1. SMP: viscoelastic vs. thermoelastic

Previous research has developed material models of a polyurethane-based SMP and SMPC (SMP resin and aramid fiber fabric) [26]. The SMP exhibits a transition from a glassy state to a rubbery state as the temperature increases, passing through a viscoelastic region. T_g for these materials is determined to be 65 °C. During the glass transition range (50 °C to 65 °C), the elastic stiffness decreases by 96 %, while damping increases by a factor of 11.

The thermoelastic and viscoelastic material models were developed for numerical analysis. The thermoelastic model only considers temperature-dependent behavior which simplifies numerical simulations. It utilized the storage modulus curve at 1 Hz and ignored viscoelastic damping effects, as shown in Fig. 16(a). On the other hand, the viscoelastic model incorporates time- and temperature-dependent properties. Experimental data obtained at different temperatures and frequencies are mapped onto a master curve using the time–temperature superposition principle, as depicted in Fig. 16(b). The thermoelastic model is used for evaluating stiffness variation whereas the viscoelastic model can simulate both stiffness and damping variation vs. time. In this research, the thermoelastic model is employed to verify the rigidization method, including static analysis and model analysis, while the viscoelastic model is employed for full transient analysis of the proposed inflatable habitat under dynamic excitations for damping measurement [29,26].

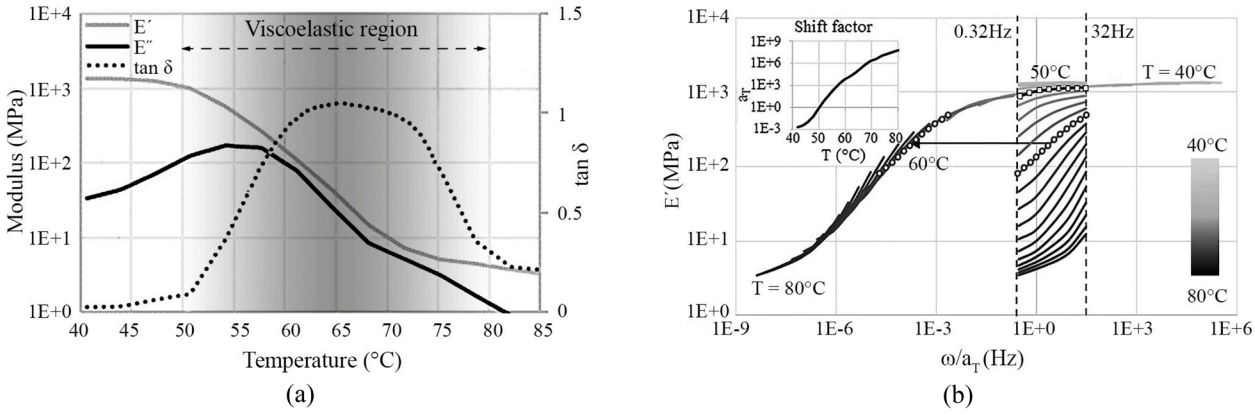

Fig. 16. SMP material characterization through DMA: (a) storage modulus (E'), loss modulus (E"), and material damping (tanδ) vs. temperature at 1 Hz; (b) master curve [26].

4.2. SMPC: thermoelastic and isotropic elastic material model

SMPs are commonly produced as composite materials to enhance their mechanical properties, particularly addressing their characteristic low stiffness and recovery stress. Continuous fiber-reinforced SMPCs offer greater resistance to impact, crashes, and fatigue, making them ideal for structural applications [30,31]. In a previous study [26], SMPC was designed as a composite skin, consisting of stacked woven aramid (Kevlar) fabric layers impregnated with SMP material. The fabric layers had fibers aligned at 0° and 90°, introducing a significant level of anisotropy.

In this case, the fabric exhibited orthotropic behavior, where the stiffness at 0° and 90° was identical. The stiffness variation capability was assessed using DMA tests, where the ratio between the glassy storage modulus (E_g) and the rubbery storage modulus (E_r) provided a measure of stiffness. Table 3 presents the stiffness properties of a single-layer SMPC [26].

A 4-layer stacking sequence ([0F/45F2/0F]) was designed to create a quasi-isotropic skin with a stiffness that is mostly unaffected by the loading direction. The skin has a modulus of approximately 8320 MPa and a thickness of 1.72 mm according to uniaxial tensile tests [26]. The ultimate tensile stress and strain, averaged over the three directions, are 107 MPa and 1.9 % respectively. Measurements using a video extensometer yielded a Poisson's ratio of 0.32. Additional angle layers can be added if stronger loads are applied.

5. Structure properties of a semi-sphere modular inflatable habitat

5.1. Numerical implementation of a semi-sphere inflatable module

In this section, a semi-sphere module is designed for numerical investigation to verify the rigidization effect and dynamic property of the inflatable structure. Specifically, a case study of one semi-sphere module was analyzed numerically, utilizing the "surface" configuration with an SMP inner shell.

When designing the dimensions of a habitat, the minimum horizontal surface area plays a crucial role. This area represents the functional area available after accounting for the reduction caused by deployed equipment, stowage, trash, and other items that decrease the usable area. In the activity area, it is essential for the vertical height to surpass 2.4 m to ensure unrestricted movement for the astronauts without being limited by the ceiling [32]. For missions lasting seven days, the standard unit is specifically designed to house a team of three astronauts. To adequately support tasks of this magnitude, a minimum area of 2.6 m^2 per crew member is necessary [33].

The proposed module in this numerical study was a semi-sphere inflatable structure with a diameter of 6 m. It included a designated area for astronauts' activities, with a vertical height exceeding 2.4 m, covering an area of 10.2 m^2. Fig. 17(a) shows the cross-section dimensions of the module. To enhance stability and functionality, the module was buried 0.5 m deep underground. The regolith layer within the inflatable structure serves two main purposes: 1) leveling the curved ground surface to create a flat foundation, especially for spherical or cylindrical modules; 2) enhancing the overall stability of the module by providing additional support and reinforcement. Regarding support condition, the bottom surface was set fixed to the ground, which means the vertical and horizontal movements were limited in this numerical model.

In the numerical simulation conducted using Ansys Workbench, three main materials were considered: 1) a flexible AFRP restraint layer, 2) an SMP/SMPC rigidization layer, and 3) a compressed regolith outer protection layer. The material properties used in the simulation were derived from testing results presented in Sections 3 and 4, as well as from relevant literature, and are summarized in Table 4 [26]. Note that a small value of 1 MPa is assigned to the nonrigid SMP to simulate a membrane without rigidization. The compressive modulus of lunar regolith was correlated with the stress level and determined based on existing literature, which recommended a compression index value of 0.05. This conversion suggested a compressive modulus range of approximately 10.7–11.3 MPa for stress levels between 0.1 and 0.2 MPa. In this numerical study, the compressive modulus of lunar regolith is assumed to be 11 MPa, while the density is reported as 1740 ± 50 based on a very dense level at a depth of 30–60 cm [34,35]. In terms of the FEM model, SOLID186 elements were used for the SMP layer, while SURF156 elements were employed to account for the membrane effect of the AFRP. The mesh sizes for SMP and regolith elements were set at 100 mm and 200 mm, respectively.

Note that in this case study temperature-induced stresses in the inner inflatable structure were not verified due to the use of a 3 m thick compacted regolith layer for thermal isolation. This layer has been proven sufficient to protect the inflatable module against extreme temperatures: approximately 253°F during the day and −243°F at night [37].

5.2. Validation of rigidization capability through static analysis: 1 atm inner pressure vs. air leakage

In this case, the SMP rigidization method was validated through a static analysis, comparing the structural behavior before and after rigidization under 1 atm internal pressure and air leakage. The membrane consisted of a 10 mm SMP layer and a 10 mm AFRP restraint layer. The 3 m thick regolith layer induced a uniform downward external pressure of 1740 kg/m^3 × 1.63 m/s^2 × 3 m = 8.1 kPa on the Moon. In addition, the inflatable module maintained an internal pressure equivalent to atmospheric level (1 atm = 101 kPa) during normal operation. Fig. 17(b) illustrates the support and static load conditions that were present during the module's service.

The structure made of nonrigid SMP material, experienced a maximum deformation of 55.2 mm and a maximum equivalent (von Mises) stress of 38.7 MPa in the AFRP and 0.37 MPa in the SMP. After rigidization, the maximum deformation decreased to 27.1 mm (reduced by 51 %), and the maximum stress in AFRP dropped to 31.1 MPa (reduced by 20 %). The rigid SMP layer took over part of the stress, resulting in an increased stress level of 20.4 MPa. Fig. 18 provides a comparison of the contour plots illustrating the deformation and stresses of nonrigid and rigid cases.

During puncture, internal pressure P_1 dropped to zero while external pressure P_2 remained constant, leading to sudden buckling and convergence failure due to excessive deformation, as shown in Fig. 19 (a). This failure occured when the internal pressure reached a level similar to the external pressure, the structure experienced compression which the flexible AFRP cannot withstand. However, in the rigidized structure after air leakage ($P_1 = 0$), the maximum deformation of the structure and equivalent stress in the SMP material were limited to 21.4 mm and 7.9 MPa, respectively, as shown in Fig. 19(b) and (c).

For crewed lunar application, the internal pressure is maintained at 1 atm, while external pressure actually benefits to balance some inner pressure, resulting in a lower stress level in the inflatable structure compared to scenarios without external pressure. In the supplementary analysis, the load-bearing capacity of the inflatable structure without a regolith protection layer was simulated using an inner pressure $P_1 = 1$ atm = 101 kPa and an external pressure $P_2 = 0$, which serves as a

Table 3
Stiffness properties of single layer SMP-aramid composite (SMPC) [26].

Specimens	0°/90° SMPC	±45° SMPC
E_g (MPa)	9600	1780
E_r (MPa)	2234	84
E_g/E_r	4	21
T_g	88 °C	76 °C

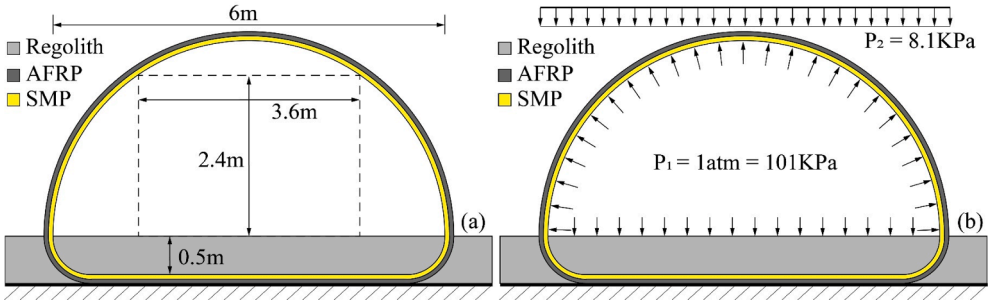

Fig. 17. Semi-sphere rigidizable inflatable module: (a)dimensions of the cross-section;(b) static load conditions in service.

Table 4
Main material properties.

Functional layers	Restraint layer	Rigidization layer SMP nonrigid	SMP rigid [26,36]	Outer protection layer
Material	Flexible AFRP	SMP/SMPC	SMP/SMPC	Regolith [34,35]
Density (kg/m^3)	1451	1050	1050	1740
FEM unit type	SURF156	SOLID186	SOLID186	SOLID186
Modulus (MPa)	8543	1	1541	11
Tensile Strength (MPa)	151	0.63	36	–

reference case. The maximum deformation observed was 68 mm, and the stress levels were within the safety range, with 47.4 for AFRP and 0.47 for SMP. In certain instances, the completed regolith outer structure can stand alone, so the inflatable structure and the regolith protection layer function as separate entities. Detailed information regarding the maximum average deformation and stresses in AFRP and SMP for both nonrigid and rigid cases under 1 atm inner pressure and air leakage conditions are reported in Table 5.

The numerical results of this section clearly demonstrate the effectiveness of the rigidizable layer in preventing structural collapse. This observation can also be extended to the terrestrial extreme environments, such as polar regions and plateaus. Without extra inner pressure, the structure solely maintains its shape under self-weight. However, the presence of additional loads, such as uniform downward snow loads in cold regions, leads to the collapse of inflatable structures. Rigidization, on the other hand, effectively mitigates these risks and ensures collapse prevention.

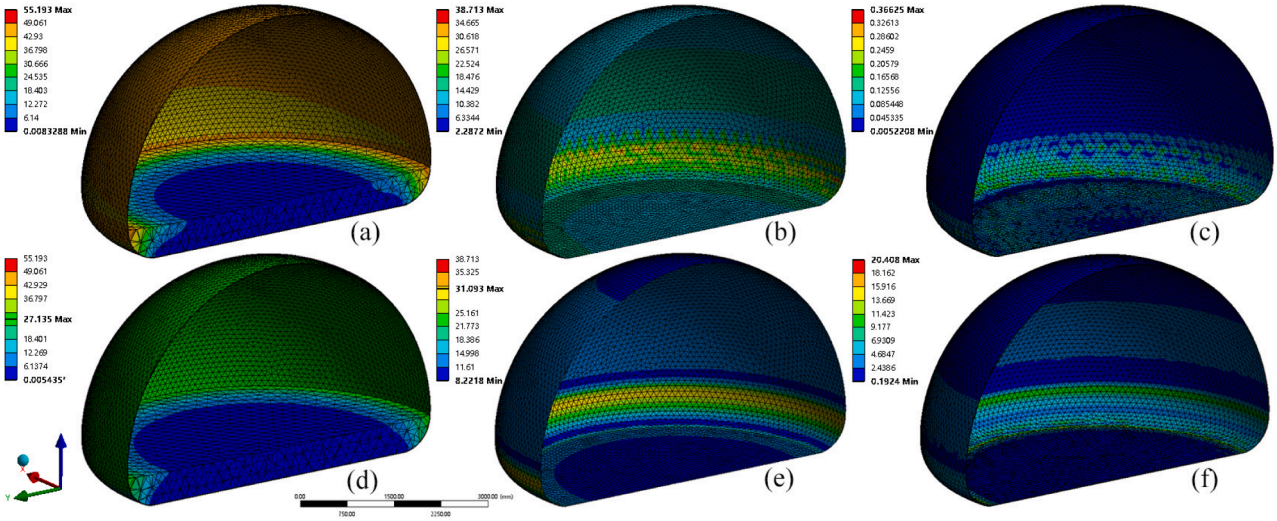

Fig. 18. Semi-sphere inflatable habitat with 1 atm inner pressure: (a) deformation, (b) AFRP stress, and (c) SMP stress at nonrigid case; (d) deformation, (e) AFRP stress, and (f) SMP stress at rigid case.

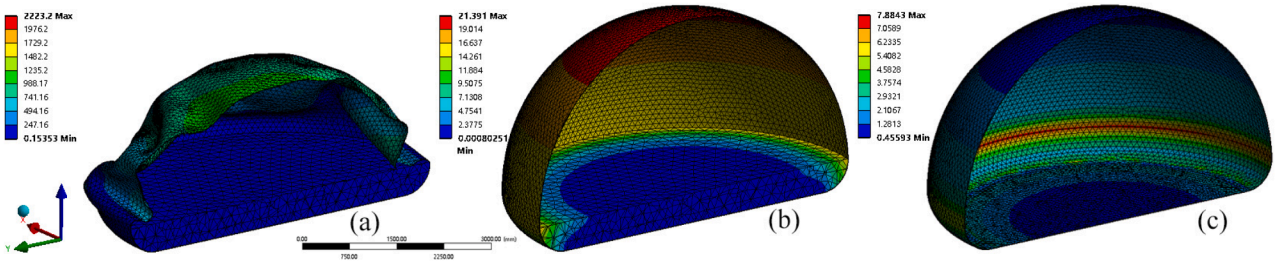

Fig. 19. Semi-sphere inflatable habitat under air leakage: (a) deformation at nonrigid (collapse occurs) case; (b) deformation and (c) SMP stress at rigid case.

Table 5
Nonrigid vs. rigidized at $P_1 = 101$ kPa inner pressure and air leakage conditions: deformations and stresses.

Conditions	$P_1 = 101$ kPa nonrigid	$P_1 = 101$ kPa and $P_2 = 8.1$ kPa		Air leakage ($P_1 = 101$ kPa to 0) and $P_2 = 8.1$ kPa	
		Nonrigid	Rigid	Nonrigid	Rigid
Deformation (mm)	68.0	55.2	27.1	Fail to converge	21.4
AFRP stress (MPa)	47.4	38.7	31.1	Fail to converge	5.4×10^{-3}
SMP stress (MPa)	0.47	0.37	20.4	Fail to converge	7.9

5.3. Frequency and damping

In this section, the dynamic properties of the inflatable structure were examined, considering three different cases: nonrigid, rigid, and viscoelastic. The nonrigid case had no rigidization layer, while the rigid and viscoelastic cases incorporated an SMP rigidization layer. In the rigid case, the SMP remained in a rigid glassy state at an ambient temperature of 25 °C, while in the viscoelastic case, it was activated to a highly damped viscoelastic region near its T_g. The assessment extends to other non-pressurized inflatable lunar modules and Earth environments. According to *DUOL Air Domes*, it is recommended to maintain a standard pressure of 0.15–0.25 kPa inside air inflated structures under normal conditions, depending on the dome size and specifications. Xue *et al.* observed in an experimental study that when the pressure difference dropped below 0.025 kPa, the inflatable structure began to collapse. Therefore, a pressure difference of 0.2 kPa was chosen to maintain the shape of the inflatable module [38].

Table 6 reports the natural frequency and frequency shift, along with the damping variation observed when the SMP layer was actuated from the ambient temperature (25 °C) to the transition temperature (65 °C) of the structure, considering the causes of inner pressures $P_1 = 101$ kPa and 0.2 kPa. Based on the modal analysis, it was observed that the first two modes primarily exhibited displacement in the top membrane portion, while the subsequent modes demonstrated significant deformation in the regolith basement. Specifically, the first mode corresponded to horizontal movement, while the second mode was characterized by vertical displacement, as shown in Fig. 20. The frequency calculations took prestress into account. In general, all cases under 1 atm inner pressure showed higher frequencies but lower frequency shifts compared to those under 0.2 kPa inner pressure. This can be attributed to the stiffening effect from inner pressure. When the SMP material operated within the viscoelastic range, the rigidized structure exhibited a smaller damping ratio under 1 atm inner pressure than under 0.2 kPa inner pressure. This difference could be attributed to the prestress effect of the inner pressure, which counteracted the inherent viscoelasticity of the SMP material.

In the full transient analysis of the inflatable structure, a viscoelastic material model is utilized. This analysis includes a free vibration test, wherein a ground displacement of 100 mm is applied to evaluate the changes in damping caused by viscoelastic effects. To determine the damping ratio ζ, the displacement logarithmic decrement $\Delta = \ln(\frac{x(t)}{x(t+1)})$ is applied to compute ζ through formula (2). In the absence of internal pressure ($P_1 = 0.2$ kPa), the maximum structural damping reached up to 1.57 % when the SMP was activated within the viscoelastic region around $T_g = 65$ °C, consistent with previous studies [29]. This highlights that the presence of a rigidization layer increases the damping of the inflatable structure.

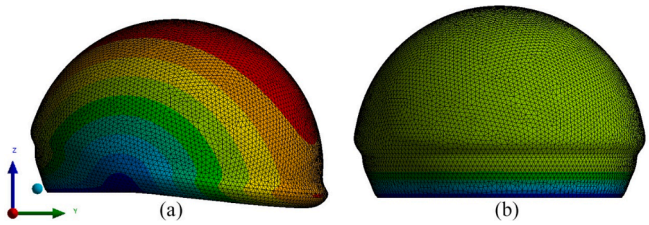

Fig. 20. Semi-sphere inflatable habitat: (a) first and (b)second modal shapes.

$$\zeta = \frac{\Delta/2\pi}{\sqrt{1 + (\Delta/2\pi)^2}} \tag{2}$$

To evaluate the load-bearing capacity of the structure when SMP is actuated to 65 °C (viscoelastic case), an additional static analysis was performed. In this analysis, an inner pressure of $P_2 = 101$ kPa was applied to simulate service conditions. The results of this analysis indicated that the inflatable structure experienced a maximum deformation of 37.4 mm. The maximum equivalent stress observed was 43.9 MPa in the AFRP material and 1.8 MPa in the SMP material. These stress values fall within the safe range, confirming that the structure can withstand the applied static load in the controlled case.

6. Discussion

Construction in extreme environments poses challenges such as harsh environments, limited local resources, costly transportation, and labor shortage. This paper focuses on lunar construction as an extreme example and proposes using rigidizable inflatable habitats as a novel structural concept and construction method. The rigidization layer, made of SMP, enables the membrane to transition between flexible and stiff states to meet different requirements during transportation, construction, and service life. The advantages of this concept can be summarized as follows:

- **Transportation and space utilization efficiency**: Considering rockets' transportation capability, structural inner atmosphere pressure, loading requirements of RLSS, power system, and other equipment, well-designed folding & inflation structural concepts can provide space for astronauts' living and research activities.
- **Utilization of novel materials**: The concept takes advantage of multiple novel materials: 1) lightweight and high-performance fiber-reinforced polymers (FRP) used as main structural materials; 2) smart materials SMP and SMPC used for rigidization; 3) in-situ

Table 6
Frequency, frequency shift, modal shape, and damping ratio at uncontrolled and controlled cases.

	$P_1 = 101$ kPa			$P_1 = 0.2$ kPa		
	Nonrigid	Rigid (25 °C)	Viscoelastic (65 °C)	Nonrigid	Rigid (25 °C)	Viscoelastic (65 °C)
ω_1 (Hz)	12.5	15.2	13.5	9.7	13.2	11.4
ω_2 (Hz)	14.7	17.8	16.0	11.4	15.4	13.2
$S_{\omega 1}$ (%)	–	21.6	8.0	–	36.1	17.5
$S_{\omega 2}$ (%)	–	21.1	8.8	–	35.1	15.8
ζ (%)	0.28	0.70	1.07	0.28	0.66	1.57

materials (regolith) used for radiation, temperature, and micrometeoroid protective layers.

- **Simplified design with SMP**: The use of SMP allows for large shape changes in structures without the need for complex mechanisms with moving parts [39]. SMP resin enables seamless attachment of SMP-aramid skin with flexible AFRP, creating a rigidizable composite membrane for inflatable structures.
- **Reversible rigidization process**: SMP's transition between the glassy and rubbery states provides a physical rigidization technology that is reversible. This allows for multiple on-ground testing, including folding & expansion tests, rigidization tests, air pressure tests, and construction demonstrations.
- **Residual stress and strain reduction**: The shape recovery effect of SMP releases stored deformation energy, which helps reduce residual stress and strain in the material. This property is particularly beneficial for shape-changing structures, such as eliminating creases in the membrane.
- **Automated construction process**: The construction process, including inflation & expansion, rigidization, regolith coverage, and pressurization, can be carried out using construction robots. The erection of internal inflatable habitats requires no extra materials except for air, making the process comparatively easy.
- **Vibration suppression**: When SMP is in the viscoelastic region around its T_g, the material damping increases significantly. This property may benefit vibration suppression under dynamic excitations induced by micrometeoroid impacts, moonquakes, and other dynamic loadings during the lunar habitats' service life. [39,29]. However, inflatables have inherent favorable dynamic responses [40–42], whether the rigidization layer could contribute to improve structural dynamic responses still needs to be further verified via dynamic analysis in this paper in Section 5.

To characterize the restraint layer and rigidization materials, uniaxial tensile tests and DMA tests were conducted. Material models derived from these tests were used for numerical investigations of a rigidizable inflatable structural module. Simulation results demonstrated that the SMP rigidization layer effectively prevents the collapse of a semi-sphere inflatable structure after air leakage and enhances its load-bearing capacity throughout its service life. Additionally, the SMP layer effectively improves the dynamic properties, especially the damping ratio. However, several important notes were made, which are outlined as follows:

- **Construction process:** The construction process follows a well-defined sequence of steps: inflation & expansion, rigidization, regolith coverage, and pressurization. However, there are unresolved issues that need attention. Ensuring safety during construction within the designated timeframe is paramount, which includes protecting against micrometeorite impacts and moonquakes, as well as maintaining a balance between the inner air pressure (P_1) and external regolith pressure (P_2). Additionally, it is crucial to establish precise task requirements for designing construction robots.
- **Regolith protection layer:** Sustainable lunar construction necessitates the utilization of in-situ resources, particularly lunar regolith, in the design plan. The design of the regolith protection layer should investigate its interactions with membrane structures, considering the roughness of lunar regolith and potential wear and tear on the membrane. Ongoing research within the team [12,13] is focused on exploring the most suitable form of the regolith protection layer and developing regolith solidification and forming techniques.
- **Detailed design:** Enhancing the conceptual framework necessitates further elaboration, particularly concerning anchoring systems for foundations, functional layout, and opening and connection designs. Although inflatable structures have good transportability and large volume-to-weight ratio in nature, the incorporation of rigidization materials increases the overall weight of the structure. To enhance structural performance, reduce weight, and minimize activation energy, it is essential to optimize the strategic arrangement of rigidization materials using suitable optimization methods. Additionally, estimation of the inflatable structure's overall volume and weight should match the existing carrying capacity of the rockets. Thoughtful design of folding patterns for transportation is essential. Addressing transportation efficiency and space utilization in future research is a critical challenge that demands attention.
- **Testing specifications:** Experimental observations at the material level have revealed that the elastic modulus is highly sensitive to the angle of the fibers. A significant reduction of 70 % in tensile modulus has been observed at 10°, significantly surpassing the stiffness reduction in rigid resins. This is attributed to the minimal constraint of flexible resins on the fiber fabric, enabling greater redistribution of fibers during tensile testing. The width of the specimen determines the number of fibers passing through the clamps, thus impacting the ultimate strength. Interestingly, the ultimate strength at 40° and 45° is higher compared to 30° and even 10°, possibly due to the symmetry of fiber distribution within the specimen. The experimental results should be considered in relation to specific loading conditions, adopting appropriate failure criteria. For instance, in this study, the ultimate stress values of specimens measured after the first elastic range were deemed meaningless, as the ultimate strain value of the overall multilayer material is based on the 0° fiber direction. While the flexible AFRP in this study adheres to FRP specifications, it exhibits fabric-like behavior, prompting future research to adopt testing specifications for coated fabrics.
- **Folding impact:** Tensile testing indicated that folding had a minor impact on flexible AFRP, primarily on the resin. To minimize this impact while maintaining folding capability, material optimization is required. One approach could involve excluding resin from the folding region, although this may result in uneven stress distribution and pose challenges during fabrication. Alternatively, in our next research, we will adopt the use of a softer and more resilient silicone as a coating, combined with aramid fibers, to create a coated fabric.
- **Adaptivity to lunar conditions:** Note that resin materials enter the glassy state and become overly rigid at extremely low temperatures, like the lunar south pole where it can drop to −163 °C. This poses a challenge when folding the membranes. To ensure successful deployment of inflatable structures, it is crucial to use resins or coatings with lower glass transition temperatures (T_g) and temperature control during construction. Consideration should be given to coating materials, such as high-phenyl silicone and fluorine rubbers, that exhibit exceptional resistance to low temperatures. Note that this study primarily focuses on the conceptual design of rigidizable inflatable habitats, which have applications not only on the lunar surface but also in extreme environments like polar regions and plateaus. Therefore, these materials were tested in terrestrial experimental environments. Further research is warranted to evaluate their performance under lunar conditions. The alternation of high and low temperatures poses a challenge in the lunar environment, necessitating a thorough investigation of material performance under such extreme conditions. Concerns arise regarding potential decreases in material properties due to fiber–matrix interfacial debonding and microcracking after temperature cycling [43]. In DMA testing in our study spanning from −140 °C to 100 °C, specimens remained intact after one temperature cycle, but the effects of multiple cycles need further exploration. Considering the

loading conditions that the membrane materials undertake tension only, cracks in the resin may marginally reduce mechanical properties under tension, with aramid fibers bearing the main load. For the rigidization layer, it contributes to a certain level of compression bearing capacity for the membrane. Cracks may cause stress concentration despite constrained propagation in compression. Further exploration is needed in future research. In addition, the effect of ultraviolet radiation on material properties depends on the radiation dose, while atomic oxygen has a minor detrimental impact on material mechanical properties [43]. Similar trends may be observed in the restraint and rigidization materials in our study. Moreover, in our previous research, aging tests were conducted on two aramid fabrics, revealing a reduction of 10 % in tensile strength and modulus after 180 days in a vacuum chamber, with the major decline occurring within the initial 30 days. For the selected material with flexible resin or surface coating, vacuum aging may result from surface coating embrittlement, altered fiber friction causing wear, or poor heat transmission leading to deformation and adhesion [13]. Consequently, future research is necessary to assess the material's adaptability to extreme lunar conditions, including temperature variations, radiation exposure, vacuum, folding fatigue, and creep behavior.

- **Lunar and terrestrial environmental disparities:** The dynamic responses of structures are significantly influenced by the disparities between lunar and terrestrial environments. Factors such as pressure differentials and gravitational acceleration contribute to variations in the loads experienced during service. Consequently, control strategies for lunar applications cannot be directly transferred from Earth structures. In general, the addition of a rigidization layer improves the structure's dynamic properties. Regarding numerical analysis, the elastic material model has limitations in simulating membrane structures. Under normal service conditions, existing elastic models can adequately simulate material behavior under tension However, for simulating structural collapse and inflation process, it is crucial to consider the material's unequal strength in tension and compression. In this case, loading conditions were tricky to ensure no compression occurring in the membrane. In the future, multibody dynamics software is also planned for further analysis.
- **Multi-level testing:** This paper focused on material-level tests, but future research should include structural-level experiments using scaled-down physical prototypes, as shown in Fig. 21. These experiments are needed to verify the folding and inflation process, rigidization capability, airtightness, and impact resistance of the inflatable structure. Furthermore, a construction demonstration is necessary to prove the feasibility of the designed construction process.

7. Conclusion

This paper proposes a new rigidizable inflatable habitatation system for lunar construction, offering advantages such as low transportation costs, easy construction, outstanding properties, and versatile applications. The conclusion can be summarized as follows:

- **System:** The proposed structure system adopts a ball-and-stick model that incorporates cylindrical and spherical basic units, allowing for the extension and construction of large lunar bases. Each module is a rigidizable inflatable structure capable of adapting to various application scenarios, such as transportation, construction, and service life, through changes in material properties. This design offers benefits such as reduced transportation costs and a straightforward construction process that can be easily coordinated with robotic automatic construction. The paper also presents an automated construction process specifically designed for this purpose.
- **Material:** The paper explores membrane materials that enable rigidization, including restraint materials and rigidization materials. It provides parameters that affect material properties and presents material design methods. Temperature primarily affects the stiffness of the resin, which, in turn, impacts the folding performance of the membrane. When the temperature falls below T_g, the membrane becomes excessively stiff to fold effectively. Furthermore, folding, even in the flexible state, can lead to resin damage, thereby compromising the load-bearing capacity of the membrane material. Based on these findings, the paper proposes performance requirements and improvement directions for materials in lunar environments, as well as research methods for materials that can serve as references for similar studies in the future.
- **Structure:** The research utilizes numerical analysis to assess the load-bearing capacity and safety of the structure under lunar service

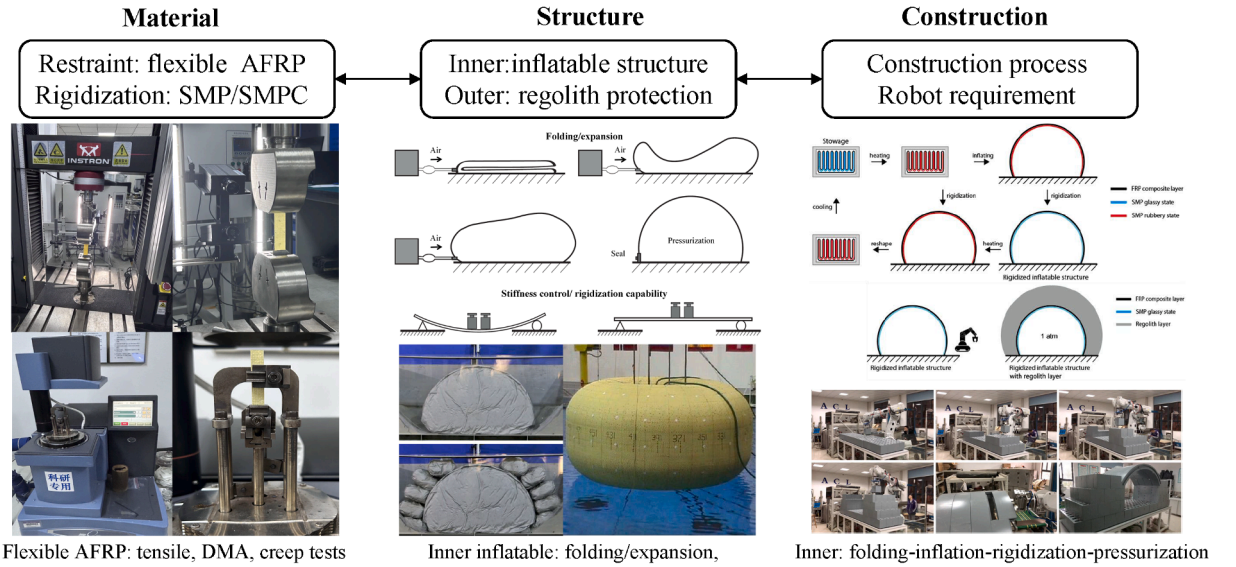

Fig. 21. Multi-level testing of rigidizable inflatable lunar habitat: material, structure [25,13], and construction [11].

conditions. This analysis serves to validate the feasibility of the concept of rigidizable inflatable habitats. The paper highlights the effectiveness of incorporating an SMP rigidization layer, which effectively prevents structural collapse and enhances structural dynamic properties. This design not only provides innovative ideas and feasible solutions for lunar base construction but also holds potential for application in other extreme environments such as Mars, polar regions, and plateaus. Furthermore, it has implications for various fields including soft robotics, intelligent buildings, and machinery.

Further in-depth design is required to address specific aspects, including energy and weight estimations, control systems, connections, and openings. Future research will focus on exploring the final geometry of habitats and the forms of the regolith layer (compacted regolith, bricks, or bags), alongside estimating transportation and space utilization efficiency. Furthermore, upcoming work also involves investigating optimal arrangements of rigidization materials, optimal design of restraint materials, material adaptation to extreme environments, and other variable stiffness systems. Additionally, prototyping, actual production, and construction demonstrations will play pivotal roles in advancing these initiatives.

CRediT authorship contribution statement

Qinyu Wang: Writing – review & editing, Writing – original draft, Visualization, Validation, Software, Resources, Methodology, Investigation, Funding acquisition, Formal analysis, Conceptualization. **Peng Feng:** Writing – review & editing, Validation, Supervision, Resources, Project administration, Methodology, Conceptualization. **Kaspar Jansen:** Visualization, Validation, Software, Methodology. **Charun Bao:** Visualization, Validation, Conceptualization.

Declaration of competing interest

The authors declare that they have no known competing financial interests or personal relationships that could have appeared to influence the work reported in this paper.

Data availability

Data will be made available on request.

Acknowledgements

This research project has been supported by National Natural Science Foundation of China (52308265) (42241109), 17th China Postdoctoral Science Foundation Fellowship (2024T170487), Guoqiang Institute, Tsinghua University (2021GQG1001), China Postdoctoral International Exchange Program (YJ20220280), and Shuimu Tsinghua Scholar Program.

Appendix

.

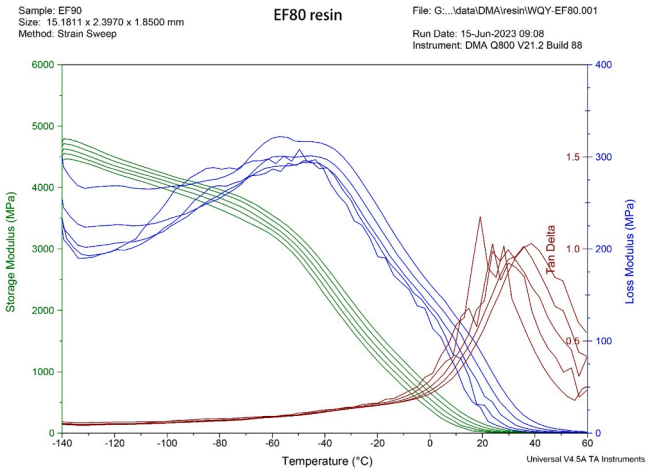

Fig. A1. Storage modulus, loss modulus, and Tan δ vs. temperature curves for flexible epoxy resin EF80.

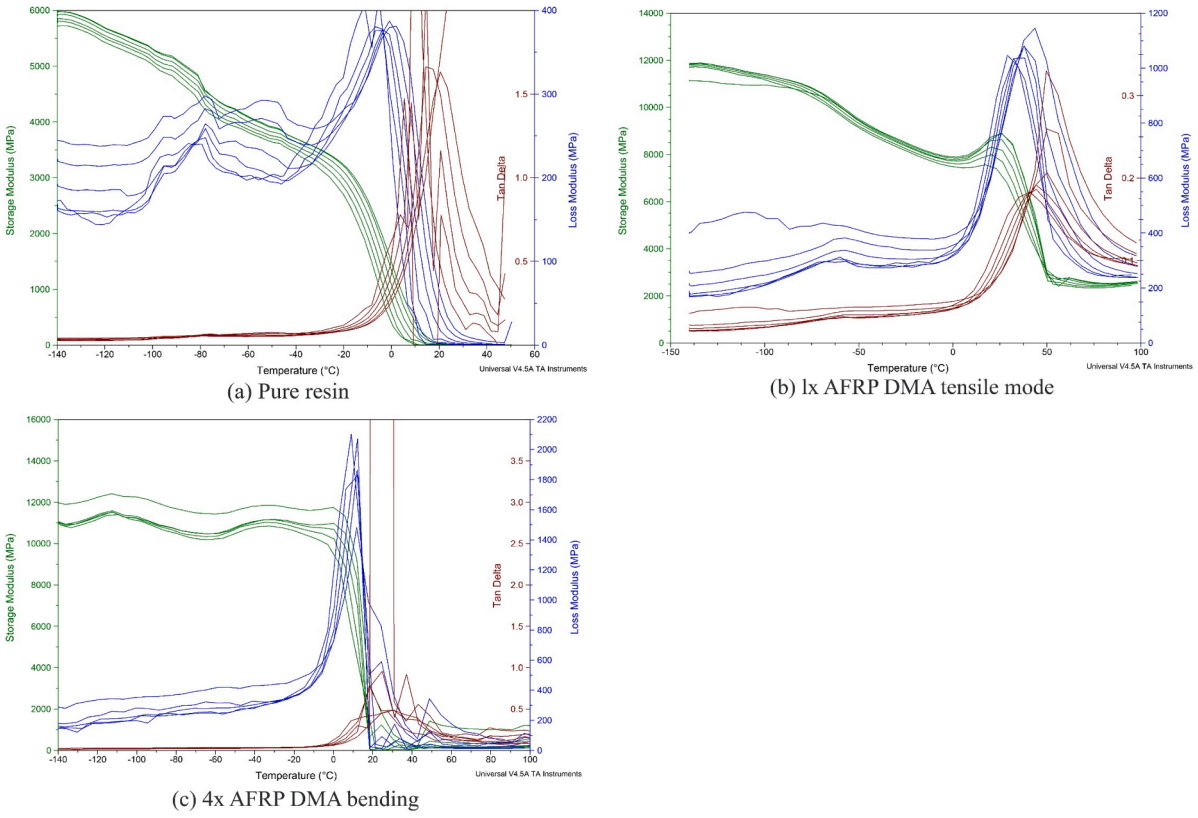

(a) Pure resin

(b) lx AFRP DMA tensile mode

(c) 4x AFRP DMA bending

Fig. A2. Storage modulus, loss modulus, and Tan δ vs. temperature for YH2130 AFRP: (a) pure resin, (c) one-layer AFRP under tensile mode, and (e) four-layer AFRP under bending mode.

References

[1] F. Ruess, J. Schaenzlin, H. Benaroya, Structural design of a lunar habitat, J. Aerosp. Eng. 19 (3) (2006) 133–157.

[2] M. Smith, D. Craig, N. Herrmann, E. Mahoney, J. Krezel, N. McIntyre and K. Goodliff, "The artemis program: An overview of nasa's activities to return humans to the moon," *2020 IEEE Aerospace Conference,* pp. 1-10.IEEE, 2020, March.

[3] J. Song, China emphasizes international cooperation in future lunar and deep space exploration, Bull. Chin. Acad. Sci. 2 (2019) 72–79.

[4] J. Flahaut, C. van der Bogert, I. Crawford, S. Vincent-Bonnieu, Scientific perspectives on lunar exploration in Europe, npj Microgravity 9 (1) (2023) 50.

[5] T. Herzig, N. Kömle, W. Macher, G. Bihari, P. Gläser, Site selection, thermodynamics, environment and life support analysis for the PneumoPlanet inflatable lunar habitat concept, Planet. Space Sci. 224 (2022) 105595.

[6] H. Sasaki and J. Director, "JAXA's Lunar exploration activities," in *Proceedings of the 62nd Session of COPUOS*, Vienna, Austria, 2019.

[7] T. Hoshino, S. Wakabayashi, M. Ohtake, Y. Karouji, T. Hayashi, H. Morimoto, H. Shiraishi, T. Shimada, T. Hashimoto, H. Inoue, R. Hirasawa, Lunar polar exploration mission for water prospection-JAXA's current status of joint study with ISRO, Acta Astronaut. 176 (2020) 52–58.

[8] H.J. An, South Korea's Space Program, Asia Policy 15 (2) (2020) 34–42.

[9] T. Rousek, K. Eriksson, O. Doule, SinterHab, Acta Astronaut. 74 (2012) 98–111.

[10] G. Cesaretti, E. Dini, X. De Kestelier, V. Colla, L. Pambaguian, Building components for an outpost on the Lunar soil by means of a novel 3D printing technology, Acta Astronaut. 93 (2014) 430–450.

[11] C. Zhou, R. Chen, J. Xu, L. Ding, H. Luo, J. Fan, E. Chen, L. Cai, B. Tang, In-situ construction method for lunar habitation: Chinese Super Mason, Autom. Constr. 104 (2019) 66–79.

[12] C. Bao, D. Zhang, Q. Wang, Y. Cui, P. Feng, Lunar In Situ Large-Scale Construction: Quantitative Evaluation of Regolith Solidification Techniques, Engineering (2024).

[13] C. Bao, P. Feng, D. Zhang, Q. Wang, S. Yang, Conceptual Design and Experimental Investigation of Regolith Bag Structures for Lunar in situ Construction, Journal of Building Engineering (2024) 110245.

[14] H. Qi, M. Yang, X. Zhang, Y. Zhang, B. Wu, J. Liu, Review on the structural design and materials of covers for inflatable lunar habitat (in Chinese), Spacecraft Environment Engineering 38 (6) (2021) 715–722.

[15] B. Defoort, V. Peypoudat, M.C. Bernasconi, K. Chuda, X. Coqueret, Recent advances in the rigidization of gossamer structures, in: Extile Composites and Inflatable Structures, 2005, pp. 259–283.

[16] M. Schenk, A.D. Viquerat, K.A. Seffen, S.D. Guest, Review of inflatable booms for deployable space structures: packing and rigidization, J. Spacecr. Rocket. 51 (3) (2014) 762–778.

[17] J. Lin, C. Knoll, C. Willey, Shape memory rigidizable inflatable (RI) structures for large space systems applications. In *47th AIAA/ASME/ASCE/AHS/ASC Structures, Structural Dynamics, and Materials Conference 14th AIAA/ASME/AHS Adaptive Structures Conference 7th*, 2006.

[18] C. Heinicke, M. Arnhof, A review of existing analog habitats and lessons for future lunar and Martian habitats, REACH 21 (2021) 100038.

[19] H. Benaroya, The evolution of lunar habitat concepts, Int. J. Space Struct. 37 (3) (2022) 187–195.

[20] A. Howe, R. Polit-Casillas, A. Austin, A. Colaprete, J. Elliott, T. Fong, S. Magnus, P. Metzger, A. Parness, H. Schmitt and B. Sherwood, "Planetary autonomous construction system (P@ X)," 2019.

[21] K.L. Ferrone, A.B. Taylor, H. Helvajian, In situ resource utilization of structural material from planetary regolith, Advances in Space Research 69 69 (5) (2022) 2268–2282.

[22] Y. Li, K. Cao, S. Lan, J. Xu, B.L.X. Chen, Design of a Light, Foldable and Flexibility Lunar Base, Aerospace China 18 (3) (2019) 32–37.

[23] A. Pronk, Y. Wu, P. Luo, Q. Li, X. Liu, S. Brands, R. Blok, Y. Dong, Design and construct of the 30.5 meter Flamenco Ice Tower, Proceedings of IASS Annual Symposia 2018 (9) (2018) 1–8.

[24] X. Fu, Y. Shi, Investigation development on space inflatable capsule (in Chinese), Spacecraft Recovery & Remote Sensing 41 (3) (2020) 37–46.

[25] G.D. Valle, D. Litteken, T.C. Jones, Review of habitable softgoods inflatable design, analysis, testing, and potential space applications, in: AIAA Scitech 2019 Forum, 2019, p. 1018.

[26] Q. Wang, G. Senatore, K. Jansen, A. Habraken, P. Teuffel, Design and characterization of variable stiffness structural joints, Mater. Des. 187 (2020) 108353.

[27] J.D. Ferry, Viscoelastic properties of polymers, John Wiley & Sons, 1980.

[28] J. Williams, B. Greenhagen, D. Paige, N. Schorghofer, E. Sefton-Nash, P. Hayne, P. Lucey, M. Siegler, K. Aye, Seasonal polar temperatures on the Moon, J. Geophys. Res. Planets 124 (10) (2019) 2505–2521.

[29] Q. Wang, G. Senatore, K. Jansen, A. Habraken, P. Teuffel, Seismic control performance of a three-story frame prototype equipped with semi-active variable stiffness and damping structural joints, Earthq. Eng. Struct. Dyn. 50 (13) (2021) 3379–3402.
[30] Y. Liu, H. Du, L. Liu, J. Leng, Shape memory polymers and their composites in aerospace applications: a review, Prog. Mater Sci. 56 (7) (2011) 1077–1135.
[31] K. Gall, M. Mikulas, N.A. Munshi, F. Beavers, M. Tupper, Carbon fiber reinforced shape memory polymer composites, J. Intell. Mater. Syst. Struct. 11 (11) (2000) 877–886.
[32] M. B. J. &. H. K. Whitmore, "NASA-STD-3001, space flight human-system standard and the human integration design handbook," *Industrial and Systems Engineering Research Conference,* pp. No. JSC-CN-25695, 2012, May.
[33] N. Handbook, "NASA Human Integration Design Handbook (HIDH)-NASA," vol. 3407, pp. SP-2010, 2010.
[34] W. Carrier III, G. Olhoeft and W. Mendell, "Physical properties of the lunar surface," *Lunar sourcebook, a user's guide to the moon,* pp. 475-594, 1991.
[35] S. W. Johnson and K. M. Chua, "Properties and mechanics of the lunar regolith," 1993.
[36] V. Kaymenaki, Numerical & Experimental Investigation of the Behavior of SMP Structural Joints, Master Thesis (2018).
[37] D.K. Kaja, Design of inflatable lunar structure, Rutgers The State University of New Jersey, School of Graduate Studies, 2017.
[38] S. Xue, F. Yan, G. Sun, Deflation and collapse of air-supported membrane structures, Thin-Walled Struct. 169 (2021) 108338.
[39] Q. Wang, G. Senatore, K. Jansen, A. Habraken, P. Teuffel, Multi-scale experimental testing on variable stiffness and damping components for semi-active structural control, Compos. Struct. 281 (2022) 114976.
[40] C. Cassapakis and M. Thomas, "Inflatable structures technology development overview," *Space programs and technologies conference,* p. 3738, 1995.
[41] H. Benaroya, Lunar habitats: A brief overview of issues and concepts, Reach 7 (2017) 14–33.
[42] L. Bowling, B. Horvath and C. Wohl, "Integration of Advanced Structures and Materials Technologies for a Robust Lunar Habitat," in *2021 IEEE Aerospace Conference (50100)*, 2021, March.
[43] Q. Tan, F. Li, L. Liu, Y. Liu, J. Leng, Effects of vacuum thermal cycling, ultraviolet radiation and atomic oxygen on the mechanical properties of carbon fiber/epoxy shape memory polymer composite, Polym. Test. 118 (2023) 107915.